



HAL
open science

Dynamic analysis of second strain gradient elasticity through a wave finite element approach

Bo Yang, Christophe Droz, Abdelmalek Zine, Mohamed Ichchou

► **To cite this version:**

Bo Yang, Christophe Droz, Abdelmalek Zine, Mohamed Ichchou. Dynamic analysis of second strain gradient elasticity through a wave finite element approach. *Composite Structures*, 2021, 263, pp.113425. 10.1016/j.compstruct.2020.113425 . hal-03160114

HAL Id: hal-03160114

<https://hal.science/hal-03160114>

Submitted on 4 Mar 2021

HAL is a multi-disciplinary open access archive for the deposit and dissemination of scientific research documents, whether they are published or not. The documents may come from teaching and research institutions in France or abroad, or from public or private research centers.

L'archive ouverte pluridisciplinaire **HAL**, est destinée au dépôt et à la diffusion de documents scientifiques de niveau recherche, publiés ou non, émanant des établissements d'enseignement et de recherche français ou étrangers, des laboratoires publics ou privés.

Dynamic Analysis of Second Strain Gradient Elasticity through a Wave Finite Element Approach

Bo Yang^a, Christophe Droz^{a,c,d}, Abdelmalek Zine^b, Mohamed Ichchou^{a,*}

^a*Vibroacoustics & Complex Media Research Group, LTDS - CNRS UMR 5513, École Centrale de Lyon, France*

^b*Institute Camille Jordan – CNRS UMR 5208, École Centrale de Lyon, France*

^c*KU Leuven, Department of Mechanical Engineering, Celestijnenlaan 300, Heverlee, Belgium*

^d*DMMS-M Lab, Flanders Make, Belgium*

Abstract

In this article, the Second Strain Gradient (SSG) theory proposed by Mindlin is used within a Wave Finite Element Method (WFEM) framework for dynamic analysis of one-dimensional Euler-Bernoulli bending beam and torsional bar. Firstly, strong forms of continuum models including governing equations and boundary conditions for bending and torsion cases, respectively, are derived using Hamilton's principle. New "non-local" Lattice Spring Models (LSM) are expounded, giving unified description of the SSG models for bending and torsion. These LSM can be regarded as a discrete micro-structural description of SSG continuum models and the resulting dynamic equations are transformed using Fourier series. Weak forms for both bending and torsion are established based on SSG theory. Subsequently, the WFEM is used to formulate the spectral problem and compute wave dispersion characteristics from one-dimensional unit-cell structures. Finally, dispersion relations and forced responses for bending and torsion in micro-sized structures are calculated by SSG and Classical Theory (CT), and some useful conclusions are discussed.

Keywords: Second Strain Gradient theory; Wave Finite Element Method; Continuum model; Lattice model; Dispersion relation; Forced response

1. Introduction

Micro-structures have been widely investigated for their dynamic behaviors [1, 2, 3]. For example, nano-sized Phononic Crystals (PCs) are studied because of their properties for manipulating acoustic and elastic waves. Initially, the research of micro-structures was mainly focused on stop band phenomena. Then, attention was devoted to wave propagation within the pass bands, such as negative refraction, super-lens effects, acoustic cloaks and so on. The exploration for quantum spin Hall effect [4] and topological insulators [5] has recently become a hot spot for current research.

It is well known that one of the noticeable features of micro-scale structures is their size-dependent mechanical behavior [6, 7], which cannot be observed in macro-structures. Classical (local) Theory (CT) fails to describe those physical phenomena in which non-local or long-range interaction plays a non-negligible role in the deformation process. There are significant differences between the behavior of micro- and macro-scale structures, such as in their dispersion relation and forced response. In order to explore the mechanism of size-dependent behaviors for micro-sized media or structure, several theories are proposed: the surface elasticity theory [8], non-local elasticity [9], couple stress theory [10] and elastic strain gradient theory [11]. Mindlin and Eshel put forward the First Strain Gradient (SG) theory that belongs to the higher-order continuum theory [12]. The link between the atomic structure of materials and the strain gradient theory is studied by Toupin and Gazis, which provided a description for the nearest and next-nearest inter-atomic interactions [13]. The existence of a cohesive force that only exists in non-centro-symmetric materials was proved. As for the force mentioned previously in centro-symmetric media or structure, Mindlin and Toupin [11]

*Corresponding author

Email address: mohamed.ichchou@ec-lyon.fr (Mohamed Ichchou)

developed the Second Strain Gradient (SSG) theory. Mindlin offered a description for the surface tension and strain at the surface of a solid plane in the mathematical framework of SSG, showing that the strain and displacement decays exponentially as the distance to the surface increases. This result was embedded into the formulation of SSG theory as a direct expression of the material surface characteristics. For the continuum model, the well known Hamiltonian principle [3] is the most general method for calculating the governing equations as well as determining the associated boundary conditions.

Besides continuum model theory, LSM theory is another analytical method to explore the dynamic behaviors of micro-structures. The material's elastic deformation is expressed through a microscopic method according to the governing equations of the lattice. Continuum governing equations of elasticity will be regarded as the limit for LSM when the infinitesimal continuous elements scales are much larger than the distances between the lattice's particles. The LSM by SSG theory relies on an assumption that the force reflects a long-range interaction between material points. The lattice particles with nearest, next-nearest and next-next-nearest neighbor interactions are a new type for elastic materials with non-local properties.

Because of the extreme complexity of geometries and forces like Van Der Waals force, static electricity and capillary force existing in micro-sized structures, the derivation of an exact theoretical solution may not be achievable for the dynamic behaviors. Thus, it is essential to develop other methods to solve the problems emerging in micro-sized structures. The Finite Element Method (FEM) is a widely used approach to explore the mechanical properties of micro-sized structures [14, 15]. But according to the FEM, the whole structure should be meshed, hence requiring excessive computational efforts. In order to optimize the traditional FEM in slender or periodic contexts, a Wave Finite Element Method (WFEM) [16, 17, 18, 19] was introduced. The research of wave propagation in periodic systems based on the Rayleigh's approach was put forward, which provided the possibility to apply approximate approaches such as the FEM in periodic structures for the propagation of wave. The view of WFEM consists in reducing the study of the whole periodic system into the spectral analysis of a single unit cell. The resulting mass matrix and stiffness matrix are post-processed to provide the dynamic stiffness matrix for the unit cell through a periodic structure theory [16]. The WFEM has been applied to solve and analyze the dynamic problems in various engineering fields, such as textile composites [20], poro-elastic media [21] or curved structures [22].

This paper presents a method which combining SSG theory with WFEM to analyse the dynamic behavior of micro-sized structures. Firstly, a continuum model for Euler-Bernoulli bending beams and torsional bars by SSG are introduced. The strong forms including governing equations and boundary conditions are illustrated by applying the variation method. Secondly, the LSM of a micro-sized Euler-Bernoulli bending beam and torsional bar are discussed. In order to build the bending and torsion lattice equations of motion for SSG theory, the LSM with the nearest, next-nearest and next-next-nearest neighbor interactions with three different coupling parameters is considered. The suggested LSM gave a unified description of the SSG model for bending and torsion. After Fourier series transforming, the continuous governing equations of motion are determined. The variational, or weak, formulations are then calculated.

The article's structure is the following: in section 2, the weak formulations of continuum model and LSM for bending and torsion are obtained using the SSG theory. Subsequently, in section 3, the direct form of the WFEM for 1D structures is reminded. The resulting dynamic stiffness matrix of a unit cell is assembled by WFEM and the spectral eigenvalue problem is solved. In section 4, dynamic behaviors in micro-sized Euler bending beam and torsional bar are calculated. Finally, some useful conclusions are presented in section 5.

2. Second Strain Gradient (SSG) Elasticity Theory

The 1D micro-sized Euler-Bernoulli bending beam continuum problems following the SSG theory are introduced firstly in this part. Starting with the strong forms, then the corresponding variational or weak formulations are presented. The bending vibration of a micro-sized Euler beam simulating a new LSM is illustrated. The proposed LSM offers a reasonable explanation of Mindlin's SSG theory and the obtained dynamic equation of motion is fully compatible. Secondly, the strong and weak formulations of 1D micro-sized torsional bar based on SSG theory are calculated, and the new LSM for torsion case by SSG theory is presented as well.

2.1. Bending Vibration for Euler-Bernoulli Beam

2.1.1. Continuum Model

Based on the SSG theory formulated by Mindlin [11], the strain energy density \bar{u} for an isotropic linearly elastic material is established as a function including the classical infinitesimal strain $\varepsilon_{ij} = \text{sym}(\nabla\mathbf{u})$, the first order strain $\eta_{ijk} = \nabla\nabla\mathbf{u}$ and the second order strain $\zeta_{ijkl} = \nabla\nabla\nabla\mathbf{u}$, in which \mathbf{u} is the displacement vector and symbol ∇ means the gradient operator, as below:

$$\begin{aligned} \bar{u} = & \frac{1}{2} \lambda \varepsilon_{ii} \varepsilon_{jj} + \mu \varepsilon_{ij} \varepsilon_{ij} + a_1 \eta_{ijj} \eta_{ikk} + a_2 \eta_{iik} \eta_{kjj} + a_3 \eta_{iik} \eta_{jjk} + a_4 \eta_{ijk} \eta_{ijk} + a_5 \eta_{ijk} \eta_{jki} + b_1 \zeta_{iijj} \zeta_{kkll} \\ & + b_2 \zeta_{ijkk} \zeta_{ijll} + b_3 \zeta_{iijk} \zeta_{jkll} + b_4 \zeta_{iijk} \zeta_{llkj} + b_5 \zeta_{iijk} \zeta_{lljk} + b_6 \zeta_{ijkl} \zeta_{ijkl} + b_7 \zeta_{ijkl} \zeta_{jkli} + c_1 \varepsilon_{ii} \zeta_{jjkk} \\ & + c_2 \varepsilon_{ij} \zeta_{ijkk} + c_3 \varepsilon_{ij} \zeta_{kkij}, \end{aligned} \quad (1)$$

where λ and μ represent the Lamé parameters related to the Young's modulus E , the Poisson's ratio ν and the shear modulus G , as $\mu = G = E/2(1 + \nu)$, $\lambda = \nu E/(1 + \nu)(1 - 2\nu)$. a_i , b_i and c_i denote the higher order parameters emerging in SSG theory. It should be pointed out that there is no mature experimental method to determine the higher order parameters. Some researchers [23] defined the parameters mentioned above in face centered cubic (fcc) materials by the Sutton-Chen potential atom method. The higher order parameters for Aluminum (Al), Copper (Cu) and Lead (Pb) are shown in Tab. 1 and Tab. 2.

Table 1: Higher order material parameters a_i (eV/Å), c_i (eV/Å).

Material	a_1	a_2	a_3	a_4	a_5	c_1	c_2	c_3
Al	0.1407	0.0027	-0.0083	0.0966	0.2584	0.5041	0.3569	0.1782
Cu	0.1833	0.0103	0.0010	0.0717	0.1891	0.8448	0.5732	0.3465
Pb	0.1039	0.0260	0.0126	0.0154	0.460	1.0991	0.6043	0.5106

Table 2: Higher order material parameters b_i (eV·Å).

Material	b_1	b_2	b_3	b_4	b_5	b_6	b_7
Al	0.7927	0.0644	-0.1943	-0.0009	0.0009	16.1566	48.5291
Cu	0.6612	0.0663	0.2062	0.0015	0.0015	12.6254	37.9402
Pb	0.2503	0.0154	0.0595	0.0007	0.007	2.7886	8.3842

In order to calculate the governing equation of a micro-sized Euler-Bernoulli bending beam, the variational principle is applied. Considering a beam on which acting a lateral distributed force $f(x, t)$. The beam length is L as shown in Fig. 1.

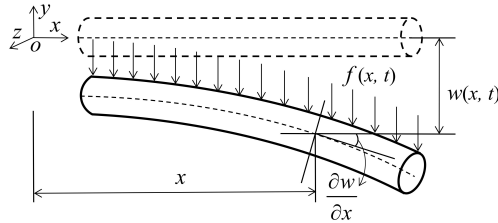


Figure 1: A Euler-Bernoulli beam under Lateral distributed force.

Assuming that the symmetry axis of the cross section coincides with the neutral axis. According to the kinematic hypothesis of the Euler-Bernoulli bending beam, the displacement fields are as follows:

$$u_1^b = -y \frac{\partial w(x, t)}{\partial x}, \quad u_2^b = w(x, t), \quad u_3^b = 0, \quad (2)$$

where u_1^b , u_2^b , and u_3^b mean the displacement components along x , y and z directions, respectively, superscript b of u represents bending case, $w(x, t)$ is the vertical displacement along y direction. Only nonzero components of displacement tensors are shown as:

$$\begin{aligned}\varepsilon_{11} &= -y \frac{\partial^2 w(x, t)}{\partial x^2}, & \eta_{111} &= -y \frac{\partial^3 w(x, t)}{\partial x^3}, & \eta_{211} &= \eta_{121} = -\frac{\partial^2 w(x, t)}{\partial x^2}, \\ \zeta_{1111} &= -y \frac{\partial^4 w(x, t)}{\partial x^4}, & \zeta_{2111} &= \zeta_{1211} = \zeta_{1121} = -\frac{\partial^3 w(x, t)}{\partial x^3}, & \zeta_{1112} &= \frac{\partial^3 w(x, t)}{\partial x^3}.\end{aligned}\quad (3)$$

Integrating the strain energy density over its volume to obtain the beam strain potential energy as:

$$\mathcal{U} = \int_0^L \int_A \bar{u} dA dx. \quad (4)$$

Whereupon, the beam strain potential energy for SSG theory can be obtained by substitution of Eq. 1 and Eq. 3 into Eq. 4:

$$\mathcal{U} = \frac{1}{2} \int_0^L \left[B_1^b \left(\frac{\partial^2 w(x, t)}{\partial x^2} \right)^2 + B_2^b \left(\frac{\partial^3 w(x, t)}{\partial x^3} \right)^2 + B_3^b \left(\frac{\partial^4 w(x, t)}{\partial x^4} \right)^2 + B_4^b \frac{\partial^2 w(x, t)}{\partial x^2} \frac{\partial^4 w(x, t)}{\partial x^4} \right] dx, \quad (5)$$

where $B_1^b = 2(a_1 - a_2 + a_3 + 3a_4 - a_5)A + EI$, $B_2^b = 2(a_1 + a_2 + a_3 + a_4 + a_5)I + 4(b_2 - b_4 + b_5 + 2b_6)A$, $B_3^b = 2(b_1 + b_2 + b_3 + b_4 + b_5 + b_6 + b_7)I$, $B_4^b = 3(c_1 + c_2 + c_3)I$, A is the area of cross section, I means the moment of inertia. On the other hand, the kinetic energy of the beam can be expressed as:

$$\mathcal{T} = \frac{1}{2} \int_0^L \rho A \left(\frac{\partial w(x, t)}{\partial t} \right)^2 dx, \quad (6)$$

where ρ denotes the linear mass density.

The work done by external classical force and higher-order forces, \mathcal{W} , can be established in the variation form as:

$$\begin{aligned}\delta \mathcal{W} &= \int_0^L f(x, t) \delta w(x, t) dx + V_0 \delta w(x, t) \Big|_{x=0}^L + M_0 \delta \left(\frac{\partial w(x, t)}{\partial x} \right) \Big|_{x=0}^L + M_1 \delta \left(\frac{\partial^2 w(x, t)}{\partial x^2} \right) \Big|_{x=0}^L \\ &\quad + M_2 \delta \left(\frac{\partial^3 w(x, t)}{\partial x^3} \right) \Big|_{x=0}^L,\end{aligned}\quad (7)$$

where V_0 and M_0 denote the classical forces, $M_{1,2}$ is the higher order end-sectional forces of the micro-beam.

Next, the Hamilton's principle is used to calculate the strong forms of the Euler-Bernoulli beam for SSG theory as follows:

$$\int_{t_1}^{t_2} (\delta \mathcal{U} - \delta \mathcal{W} - \delta \mathcal{T}) dt = 0, \quad (8)$$

where $\delta \mathcal{U}$ is the variational form of strain energy, $\delta \mathcal{T}$ means the variational form of kinetic energy. Then doing mathematical calculations according to the variation method by substituting equations Eq. 5, 6, and 7 into Eq. 8, one obtains:

$$B_1^b \frac{\partial^4 w(x, t)}{\partial x^4} + (B_4^b - B_2^b) \frac{\partial^6 w(x, t)}{\partial x^6} + B_3^b \frac{\partial^8 w(x, t)}{\partial x^8} - f(x, t) = \rho A \frac{\partial^2 w(x, t)}{\partial t^2}. \quad (9)$$

Additionally, the boundary conditions at the ends of Euler-Bernoulli beam for SSG theory are extracted:

$$\begin{aligned}
& -B_1^b \frac{\partial^3 w(x,t)}{\partial x^3} - (B_4^b - B_2^b) \frac{\partial^5 w(x,t)}{\partial x^5} - B_3^b \frac{\partial^7 w(x,t)}{\partial x^7} = V_0 \quad \text{or} \quad \delta w(x,t) = 0, \quad \text{on} \quad \Omega = \{0, L\}; \\
& -B_1^b \frac{\partial^2 w(x,t)}{\partial x^2} - (B_4^b - B_2^b) \frac{\partial^4 w(x,t)}{\partial x^4} + B_3^b \frac{\partial^6 w(x,t)}{\partial x^6} = M_0 \quad \text{or} \quad \delta \frac{\partial w(x,t)}{\partial x} = 0, \quad \text{on} \quad \partial\Omega; \\
& -\left(\frac{1}{2}B_4^b - B_2^b\right) \frac{\partial^3 w(x,t)}{\partial x^3} + B_3^b \frac{\partial^5 w(x,t)}{\partial x^5} = M_1 \quad \text{or} \quad \delta \frac{\partial^2 w(x,t)}{\partial x^2} = 0, \quad \text{on} \quad \partial\Omega; \\
& \frac{1}{2}B_4^b \frac{\partial^2 w(x,t)}{\partial x^2} + B_3^b \frac{\partial^4 w(x,t)}{\partial x^4} = M_2 \quad \text{or} \quad \delta \frac{\partial^3 w(x,t)}{\partial x^3} = 0, \quad \text{on} \quad \partial\Omega.
\end{aligned} \tag{10}$$

Then, transforming strong form into weak form. In the FEM, the displacement $w(x, t)$ inside of an element at point $x \in R^2$ could be expressed by providing the values \mathbf{u}^b of nodal degree of freedoms (DOFs) vector and shape function $\mathbf{N}^b(x)$, as follows:

$$w(x, t) = \mathbf{N}^b(x)\mathbf{u}^b(t), \tag{11}$$

where the sizes of \mathbf{u}^b and \mathbf{N}^b are $p \times 1$ and $1 \times p$, respectively, and p means the DOFs number. In Eq. 11, the form of the interpolation function determines \mathbf{u}^b , \mathbf{N}^b and p . The C^3 continuum Hermite interpolation function that guarantees the higher-order strain field and displacement field smooth and continuous is used in Eq. 11. The nodal DOFs, nodal numbers and coordinate of 1D Hermite element are presented in Fig. 2. For 1D C^3 continuum Hermite element (element length is d_e), there are four DOFs, $w_i, \theta_i, \frac{\partial^2 w_i}{\partial x^2}, \frac{\partial^3 w_i}{\partial x^3}, i = 1, 2$, on each node. The Hermite shape functions

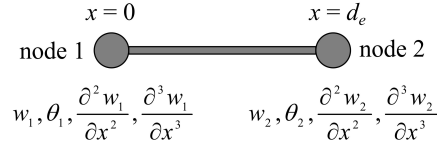


Figure 2: Definition of nodal DOFs, nodal numbers and coordinate for 1D.

corresponding to the eight DOFs of the 1D element are expressed as:

$$\begin{aligned}
\mathbf{N}_1^0 &= 1 - 35x^4/d_e^4 + 84x^5/d_e^5 - 70x^6/d_e^6 + 20x^7/d_e^7, \quad \mathbf{N}_2^0 = 35x^4/d_e^4 - 84x^5/d_e^5 + 70x^6/d_e^6 - 20x^7/d_e^7, \\
\mathbf{N}_1^1 &= x - 20x^4/d_e^3 + 45x^5/d_e^4 - 36x^6/d_e^5 + 10x^7/d_e^6, \quad \mathbf{N}_2^1 = -15x^4/d_e^3 + 39x^5/d_e^4 - 34x^6/d_e^5 + 10x^7/d_e^6, \\
\mathbf{N}_1^2 &= x^2/2 - 5x^4/d_e^2 + 10x^5/d_e^3 - 15x^6/d_e^4 + 2x^7/d_e^5, \quad \mathbf{N}_2^2 = 5x^4/d_e^2 - 7x^5/d_e^3 + 13x^6/d_e^4 - 2x^7/d_e^5, \\
\mathbf{N}_1^3 &= x^3/6 - 2x^4/3d_e + x^5/d_e^2 - 2x^6/3d_e^3 + x^7/6d_e^4, \quad \mathbf{N}_2^3 = -x^4/6d_e + x^5/2d_e^2 - x^6/2d_e^3 + x^7/6d_e^4,
\end{aligned} \tag{12}$$

where the subscript and superscript of \mathbf{N} in Eq. 12 denote the nodal numbers and the order of the derivative with respect to coordinate $x \in [0, d_e]$, respectively. Substituting Eq. 11 into equilibrium equation Eq. 9, then doing integration to the resulting formula by the Galerkin's approach leads to:

$$\begin{aligned}
& \left[\int_0^{d_e} (\mathbf{N}^b)^T \left(B_1^b \frac{d^4 \mathbf{N}^b}{dx^4} + (B_4^b - B_2^b) \frac{d^6 \mathbf{N}^b}{dx^6} + B_3^b \frac{d^8 \mathbf{N}^b}{dx^8} \right) dx \right] \mathbf{u}^b - \int_0^{d_e} (\mathbf{N}^b)^T f(x, t) dx \\
& = \left(\int_0^{d_e} (\mathbf{N}^b)^T \rho A \mathbf{N}^b dx \right) \ddot{\mathbf{u}}^b,
\end{aligned} \tag{13}$$

in which the dot symbol over \mathbf{u}^b indicates the second derivative with respect to the time. In order to illustrate the weak form of Eq. 9, the part-by-part integration is used and result in:

$$\mathbf{K}^b \mathbf{u}^b - \mathbf{F}^b = \mathbf{M}^b \ddot{\mathbf{u}}^b, \tag{14}$$

where \mathbf{K}^b and \mathbf{M}^b represent the stiffness matrix and mass matrix, respectively, \mathbf{F}^b denotes the force vector for bending.

The aforementioned parameters are derived as:

$$\begin{aligned}
\mathbf{M}^b &= \rho A \int_0^{d_e} (\mathbf{N}^b)^T \mathbf{N}^b dx, \\
\mathbf{K}^b &= \int_0^{d_e} \left[B_1^b ((\mathbf{N}^b)'')^T (\mathbf{N}^b)'' + (B_2^b - B_4^b) ((\mathbf{N}^b)'''')^T (\mathbf{N}^b)'''' + B_3^b ((\mathbf{N}^b)'''')^T (\mathbf{N}^b)'''' \right] dx, \\
\mathbf{F}^b &= \int_0^{d_e} (\mathbf{N}^b)^T f(x, t) dx + V_0 \mathbf{N}^b |_{\partial\Omega_{V_0}} + M_0 (\mathbf{N}^b)' |_{\partial\Omega_{M_0}} + M_1 (\mathbf{N}^b)'' |_{\partial\Omega_{M_1}} + M_2 (\mathbf{N}^b)''' |_{\partial\Omega_{M_2}}.
\end{aligned} \tag{15}$$

where superscript (') is the partial derivative with respect to coordinate x . It is noted that ensuring the correctness of the correspondent relations between the local numbering and global numbering of DOFs is a prerequisite, especially owing to the strict regularity of basis functions.

2.1.2. Lattice Spring Model (LSM)

In this part, the fundamentals of Euler–Bernoulli theory and “non-local” LSM are used to discretize the beam into a series of identical elements, as shown in Fig. 3, P is the total number of lattice nodes. This LSM can reflect the mechanical response of the continuum structure when the length between each node at small scale and P is large enough. The DOFs on each node are displacement in y direction and rotation angle in $x0y$ plane. From Fig. 3(b), 3(c), 3(d), the total rotation angle of node n can be presented by displacement components as:

$$\Delta\theta_i = \frac{w_{n+i} - w_n}{id} - \frac{w_n - w_{n-i}}{id}, (i = 1, 2, 3). \tag{16}$$

The governing equation of motion at node n for a LSM of Euler beam can be illustrated by applying Lagrange

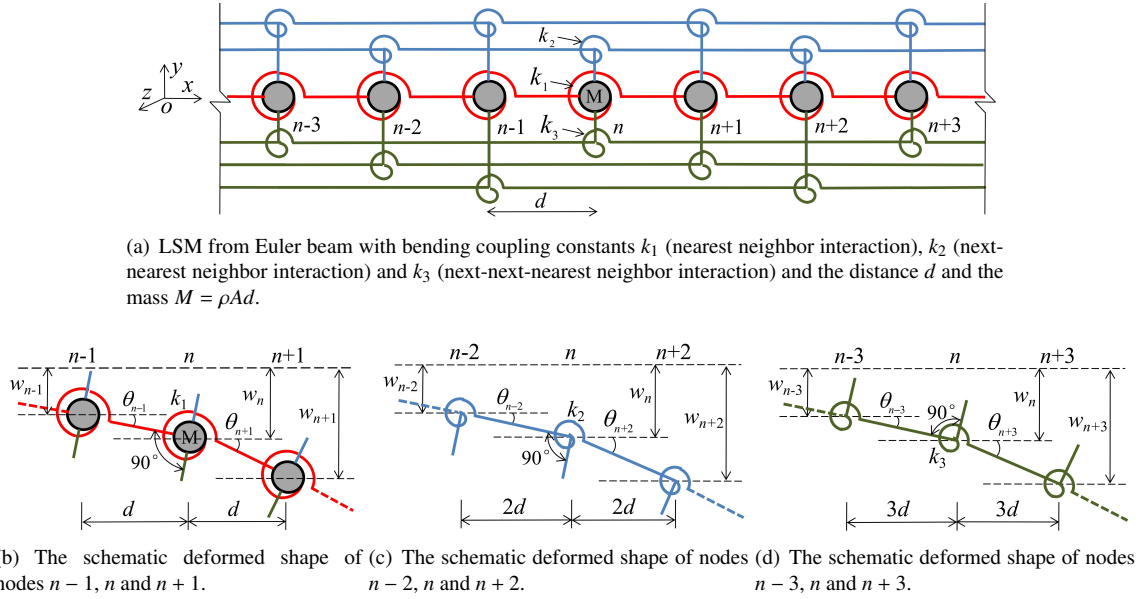


Figure 3: Sketch of a LSM beam.

equation [24] in y direction as:

$$\frac{\partial \mathcal{L}}{\partial w_n} - F_n = \frac{d}{dt} \left(\frac{\partial \mathcal{L}}{\partial \dot{w}_n} \right), \tag{17}$$

where F_n is an externally load applied at node n in y direction. $\mathcal{L}=\mathcal{T}-\mathcal{U}$ means the lagrangian that composed of the kinetic energy (\mathcal{T}) and potential energy (\mathcal{U}), where,

$$\begin{aligned}\mathcal{T} &= \frac{1}{2}M \sum_{n=1}^P \dot{w}_n^2, \\ \mathcal{U} &= \frac{1}{2}k_1 \sum_{n=1}^P (\Delta\theta_1)^2 + \frac{1}{2}k_2 \sum_{n=1}^P (\Delta\theta_2)^2 + \frac{1}{2}k_3 \sum_{n=1}^P (\Delta\theta_3)^2.\end{aligned}\quad (18)$$

The lattice equation of motion for node n can be calculated by replacing Eq. 16 and Eq. 18 into Eq. 17 as:

$$\begin{aligned}\frac{k_1}{d^3} (w_{n-2} - 4w_{n-1} + 6w_n - 4w_{n+1} + w_{n+2}) + \frac{k_2}{(2d)^3} (w_{n-4} - 4w_{n-2} + 6w_n - 4w_{n+2} + w_{n+4}) \\ + \frac{k_3}{(3d)^3} (w_{n-6} - 4w_{n-3} + 6w_n - 4w_{n+3} + w_{n+6}) - F_n = M \frac{d^2 w_n(t)}{dt^2}.\end{aligned}\quad (19)$$

Subsequently, the Fourier series transform approach is used to derive a continuous equation $w(x, t)$ from the LSM $w_n(t)$. The process from a LSM to a continuum model was defined as [25]:

(1) Assuming $w_n(t)$ is the Fourier coefficient of field $\widehat{w}(\kappa, t)$, and defining \mathfrak{F}_Δ as the Fourier series transform:

$$\widehat{w}(\kappa, t) = \sum_{n=-\infty}^{+\infty} w_n(t) e^{-i\kappa x_n} = \mathfrak{F}_\Delta (w_n(t)), \quad (20)$$

(2) Using Taylor series expansion for sine function by limiting $d \rightarrow 0$:

$$\widetilde{w}(\kappa, t) = \lim_{d \rightarrow 0} \widehat{w}(\kappa, t), \quad (21)$$

(3) The inverse Fourier transform \mathfrak{F}^{-1} :

$$w(x, t) = \frac{1}{2\pi} \int_{-\infty}^{+\infty} \widetilde{w}(x, t) e^{i\kappa x} d\kappa = \mathfrak{F}^{-1} (\widetilde{w}(x, t)), \quad (22)$$

where $x_n = dn$, κ is defined as wavenumber which will be discussed in Sec. 3. These three steps aforementioned was proved in [25, 26]. And the detail for calculating dynamic continuum equation $w(x, t)$ from LSM addressed in Appendix A, as a result:

$$\begin{aligned}G_4^b \frac{\partial^4 w(x, t)}{\partial x^4} + G_6^b \frac{\partial^6 w(x, t)}{\partial x^6} + G_8^b \frac{\partial^8 w(x, t)}{\partial x^8} + \mathcal{O}\left(G_i^b \frac{\partial^i w(x, t)}{\partial x^i}\right) - f(x, t) \\ = \rho A \frac{\partial^2 w(x, t)}{\partial t^2}, (i = 10, 12, \dots),\end{aligned}\quad (23)$$

with $G_4^b = k_1 + 2k_2 + 3k_3$, $G_6^b = -\left(\frac{k_1}{6} + \frac{4k_2}{3} + \frac{9k_3}{2}\right)d^2$, $G_8^b = \left(\frac{k_1}{80} + \frac{2k_2}{5} + \frac{243k_3}{80}\right)d^4$, $G_{10}^b = -\left(\frac{17k_1}{30240} + \frac{68k_2}{945} + \frac{1377k_3}{1120}\right)d^6, \dots$

The convergence condition for Eq. 23 is defined as:

$$\left| G_{10}^b \frac{\partial^{10} w(x, t)}{\partial x^{10}} \right| \left| G_8^b \frac{\partial^8 w(x, t)}{\partial x^8} \right| < 1. \quad (24)$$

For the continuum model of Eq. 23, the displacement solution is $w(x, t) = w_0 e^{i(\omega t - \kappa x)}$ [27], where w_0 is amplitude, ω means angular frequency. Replacing this solution into Eq. 24, as a result: the Eq. 24 holds when the node number $P \geq \pi + 1$ (here P should be infinite or large enough), then ignore higher order part, Eq. 23 will be written as:

$$G_4^b \frac{\partial^4 w(x, t)}{\partial x^4} + G_6^b \frac{\partial^6 w(x, t)}{\partial x^6} + G_8^b \frac{\partial^8 w(x, t)}{\partial x^8} - f(x, t) = \rho A \frac{\partial^2 w(x, t)}{\partial t^2}. \quad (25)$$

Compare Eq. 25 with the equation of motion from Mindlin's theory (Eq. 9), the first 3 parts should be:

$$G_4^b = B_1^b, \quad G_6^b = B_4^b - B_2^b, \quad G_8^b = B_3^b, \quad (26)$$

with $k_1 = \frac{3B_1^b}{2} + \frac{13(B_4^b - B_2^b)}{4d^2} + \frac{10B_3^b}{3d^4}$, $k_2 = -\frac{3B_1^b}{10} - \frac{2(B_4^b - B_2^b)}{d^2} - \frac{8B_3^b}{3d^4}$, $k_3 = \frac{B_1^b}{30} + \frac{(B_4^b - B_2^b)}{4d^2} + \frac{2B_3^b}{3d^4}$. Then, replacing Eq. 26 into Eq. 15, the weak formulations for Euler–Bernoulli beam from LSM will be derived finally.

2.2. Torsional Vibration for a Bar

2.2.1. Continuum Model

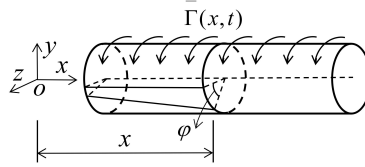


Figure 4: A torsional bar under torque.

In order to calculate the governing equation of a micro-sized torsional bar, the variational principle is applied. Considering a bar on which acting distributed torque $\bar{\Gamma}(x, t)$. The bar length is L as shown in Fig. 4. Assuming that the symmetry axis of the cross section coincides with the neutral axis. Then, the components of the displacements are expressed as:

$$u_1^t = 0, \quad u_2^t = z\varphi(x, t), \quad u_3^t = -y\varphi(x, t), \quad (27)$$

where u_1^t , u_2^t , and u_3^t represent the displacement along the directions x , y , and z , respectively, superscript t of u denotes torsional case. Therefore, the only nonzero components of displacement tensors are expressed as:

$$\begin{aligned} \varepsilon_{12} = \varepsilon_{21} &= \frac{1}{2}z \frac{\partial \varphi(x, t)}{\partial x}, \quad \varepsilon_{13} = \varepsilon_{31} = -\frac{1}{2}y \frac{\partial \varphi(x, t)}{\partial x}, \quad \eta_{112} = z \frac{\partial^2 \varphi(x, t)}{\partial x^2}, \quad \eta_{113} = -y \frac{\partial^2 \varphi(x, t)}{\partial x^2}, \\ \eta_{123} = \eta_{213} &= -\frac{\partial \varphi(x, t)}{\partial x}, \quad \eta_{132} = \eta_{312} = \frac{\partial \varphi(x, t)}{\partial x}, \quad \zeta_{1112} = z \frac{\partial^3 \varphi(x, t)}{\partial x^3}, \quad \zeta_{1113} = -y \frac{\partial^3 \varphi(x, t)}{\partial x^3}, \\ \zeta_{3112} = \zeta_{1312} &= \zeta_{1132} = \frac{\partial^2 \varphi(x, t)}{\partial x^2}, \quad \zeta_{2113} = \zeta_{1213} = \zeta_{1123} = -\frac{\partial^2 \varphi(x, t)}{\partial x^2}. \end{aligned} \quad (28)$$

In this step, the Hamilton principle is used to calculate the strong forms of a torsional bar for SSG theory. The detail addressed in Appendix B, one arrives:

$$B_1^t \frac{\partial^2 \varphi(x, t)}{\partial x^2} + (B_4^t - B_2^t) \frac{\partial^4 \varphi(x, t)}{\partial x^4} + B_3^t \frac{\partial^6 \varphi(x, t)}{\partial x^6} - \bar{\Gamma}(x, t) = \rho J \frac{\partial^2 \varphi(x, t)}{\partial t^2}. \quad (29)$$

where $B_1^t = GJ + 2A(4a_4 - a_5)$, $B_2^t = J(a_3 + a_4)/2 - 2A(b_4 + 2b_5 - 6b_6 + 2b_7)$, $B_3^t = 2J(b_5 + b_6)$, $B_4^t = Jc_3$, J means torsion of inertia within plane yOz . Additionally, the boundary conditions at the ends of bar for SSG theory are extracted:

$$\begin{aligned} B_1^t \frac{\partial \varphi(x, t)}{\partial x} + (B_4^t - B_2^t) \frac{\partial^3 \varphi(x, t)}{\partial x^3} + B_3^t \frac{\partial^5 \varphi(x, t)}{\partial x^5} &= \Gamma_0 \quad \text{or} \quad \delta \varphi(x, t) = 0, \quad \text{on} \quad \Omega = \{0, L\}; \\ (B_2^t - \frac{1}{2}B_4^t) \frac{\partial^2 \varphi(x, t)}{\partial x^2} + B_3^t \frac{\partial^4 \varphi(x, t)}{\partial x^4} &= \Gamma_1 \quad \text{or} \quad \delta \frac{\partial \varphi(x, t)}{\partial x} = 0, \quad \text{on} \quad \partial\Omega; \\ \frac{1}{2}B_4^t \frac{\partial \varphi(x, t)}{\partial x} + B_3^t \frac{\partial^3 \varphi(x, t)}{\partial x^3} &= \Gamma_2 \quad \text{or} \quad \delta \frac{\partial^2 \varphi(x, t)}{\partial x^2} = 0 \quad \text{on} \quad \partial\Omega, \end{aligned} \quad (30)$$

where Γ_0 and $\Gamma_{1,2}$ denote the classical and higher-order end-sectional loads of the micro-bar respectively.

In the FEM, the torsional angle $\varphi(x, t)$ inside of an element at point $x \in R^2$ could be expressed by providing the

values $\mathbf{u}^t(t)$ of nodal DOFs vector and the shape function $\mathbf{N}^t(x)$, as follows:

$$\varphi(x, t) = \mathbf{N}^t(x)\mathbf{u}^t(t) \quad (31)$$

where the sizes of \mathbf{u}^t and \mathbf{N}^t are $r \times 1$ and $1 \times r$, respectively, and r means the DOFs number. In Eq. 31, the form of the interpolation function determines \mathbf{u}^t , \mathbf{N}^t and r . Here, different from bending case, there are three DOFs, $\varphi_i, \frac{\partial \varphi_i}{\partial x}, \frac{\partial^2 \varphi_i}{\partial x^2}, i = 1, 2$, on each node, so the C^2 continuum Hermite interpolation function can guarantee the continuity of high-order displacement. The nodal DOFs, nodal numbers and coordinate of 1D Hermite element are presented in Fig. 5 and Hermite shape functions corresponding to the six DOFs of the 1D element are expressed as:

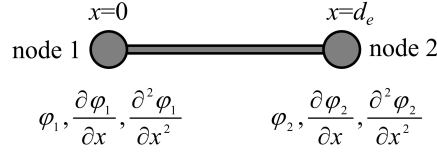


Figure 5: Definition of nodal DOFs, nodal numbers and coordinate for 1D.

$$\begin{aligned} \mathbf{N}_1^0 &= 1 - 10x^3/d_e^3 + 15x^4/d_e^4 - 6x^5/d_e^5, & \mathbf{N}_2^0 &= 10x^3/d_e^3 - 15x^4/d_e^4 + 6x^5/d_e^5, \\ \mathbf{N}_1^1 &= x/d_e - 6x^3/d_e^3 + 8x^4/d_e^4 - 3x^5/d_e^5, & \mathbf{N}_2^1 &= -4x^3/d_e^3 + 7x^4/d_e^4 - 3x^5/d_e^5, \\ \mathbf{N}_1^2 &= x^2/2d_e^2 - 3x^3/2d_e^3 + 3x^4/2d_e^4 - x^5/2d_e^5, & \mathbf{N}_2^2 &= x^3/2d_e^3 - x^4/d_e^4 + x^5/2d_e^5. \end{aligned} \quad (32)$$

According to the Galerkin's method, doing the same calculating progress as shown in bending case, the stiffness \mathbf{K}^t , mass matrices \mathbf{M}^t and force vector \mathbf{F}^t for torsion are derived as:

$$\begin{aligned} \mathbf{M}^t &= \rho J \int_0^{d_e} (\mathbf{N}^t)^T \mathbf{N}^t dx, \\ \mathbf{K}^t &= \int_0^{d_e} \left[B_1^t \left((\mathbf{N}^t)' \right)^T (\mathbf{N}^t)' + (B_2^t - B_4^t) \left((\mathbf{N}^t)'' \right)^T (\mathbf{N}^t)'' + B_3^t \left((\mathbf{N}^t)''' \right)^T (\mathbf{N}^t)''' \right] dx, \\ \mathbf{F}^t &= \int_0^{d_e} \bar{\Gamma}(x, t) \mathbf{N}^t dx + \Gamma_0 \mathbf{N}^t|_{\partial \Omega_{r_0}} + \Gamma_1 (\mathbf{N}^t)'|_{\partial \Omega_{r_1}} + \Gamma_2 (\mathbf{N}^t)''|_{\partial \Omega_{r_2}}. \end{aligned} \quad (33)$$

2.2.2. Lattice Spring Model (LSM)

In this part, the fundamentals of “non-local” LSM are used to disperse the torsional bar into a series of identical elements, as shown in Fig. 6, P is the total number of the lattice nodes. This LSM for torsional bar can reflect

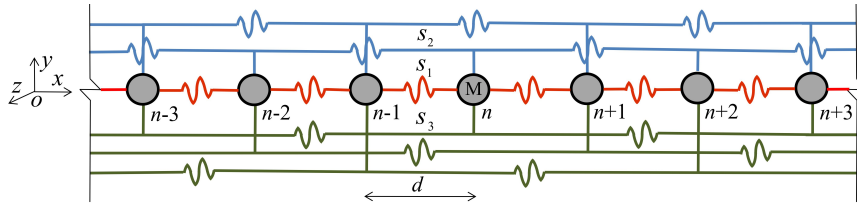


Figure 6: LSM for a torsional bar with torsional coupling constants s_1 (nearest-neighbor interaction), s_2 (next-nearest-neighbor interaction) and s_3 (next-next-nearest-neighbor interaction) and the distance d and the mass $M = \rho Ad$.

the mechanical response of the continuum structure when the length between each node at small scale and P is large enough. The lattice equation of motion for node n as:

$$s_1(\varphi_{n-1} - 2\varphi_n + \varphi_{n+1}) + s_2(\varphi_{n-2} - 2\varphi_n + \varphi_{n+2}) + s_3(\varphi_{n-3} - 2\varphi_n + \varphi_{n+3}) - \Gamma_n = \frac{mJ}{A} \frac{d^2 \varphi_n(t)}{dt^2}. \quad (34)$$

Subsequently, the Fourier series transform approach [25] is used to derive a continuous equation $\varphi(x, t)$ from the LSM $\varphi_n(t)$. The detail addressed in Appendix C, as a result:

$$\begin{aligned} & G_2^t \frac{\partial^2 \varphi(x, t)}{\partial x^2} + G_4^t \frac{\partial^4 \varphi(x, t)}{\partial x^4} + G_6^t \frac{\partial^6 \varphi(x, t)}{\partial x^6} + O\left(G_i^t \frac{\partial^i \varphi(x, t)}{\partial x^i}\right) - \bar{\Gamma}(x, t) \\ & = \rho J \frac{d^2 \varphi(x, t)}{dt^2}, (i = 8, 10, \dots), \end{aligned} \quad (35)$$

with $G_2^t = (s_1 + 4s_2 + 9s_3)d$, $G_4^t = \left(\frac{s_1}{12} + \frac{4s_2}{3} + \frac{27s_3}{4}\right)d^3$, $G_6^t = \left(\frac{s_1}{360} + \frac{8s_2}{54} + \frac{81s_3}{40}\right)d^5$, $G_8^t = \left(\frac{7s_1}{20160} + \frac{4s_2}{315} + \frac{729s_3}{2240}\right)d^7, \dots$

Here, the convergence condition is same as bending case: $P \geq \pi + 1$. Ignore higher order part, Eq. 35 will be written:

$$G_2^t \frac{\partial^2 \varphi(x, t)}{\partial x^2} + G_4^t \frac{\partial^4 \varphi(x, t)}{\partial x^4} + G_6^t \frac{\partial^6 \varphi(x, t)}{\partial x^6} - \bar{\Gamma}(x, t) = \rho J \frac{d^2 \varphi(x, t)}{dt^2}, \quad (36)$$

Compare Eq. 36 with the equation of motion for torsion from Mindlin's theory (Eq. 29), the first 3 parts should be same:

$$G_2^t = B_1^t, \quad G_4^t = B_4^t - B_2^t, \quad G_6^t = B_3^t, \quad (37)$$

with $s_1 = \frac{3B_1^t}{2d} + \frac{13(B_2^t - B_4^t)}{2d^3} + \frac{15B_3^t}{d^5}$, $s_2 = -\frac{3B_1^t}{20d} - \frac{2(B_2^t - B_4^t)}{d^3} - \frac{6B_3^t}{d^5}$, $s_3 = \frac{B_1^t}{90} + \frac{(B_2^t - B_4^t)}{6d^3} + \frac{B_3^t}{d^5}$. Replacing Eq. 37 into Eq. 33, the weak formulations for torsional bar from LSM will be derived finally.

3. Wave Finite Element Method (WFEM) for One-dimensional Structure

The WFEM offers a numerical wave characterization of periodic structures that composed of identical unit cells coupled together. In my work, one-dimensional periodic structures are considered only. The advantage of WFEM is modeling a unit cell by the conventional finite elements, which thus complex geometries or several materials can be involved. What is more, the wave propagation of whole structure can be evaluated by analyzing a single unit cell. The size of numerical problem that related directly to the number of DOFs will be reduced, thus computational time will be saved. Considering an elastic structure with identical unit cells that arranged in x direction, as presented in Fig. 7, the length of each unit cell is L_u , which corresponds to a small length of wave-guide or a unit length of periodic structure.

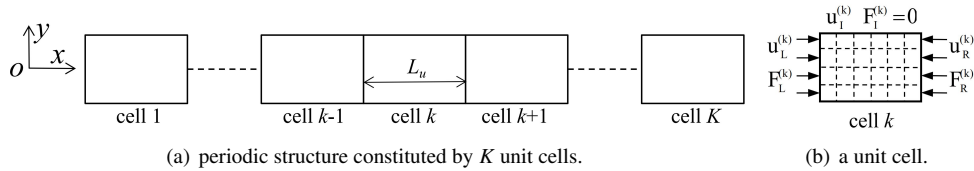


Figure 7: One-dimensional FE model for a periodic structure.

According to the WFEM, only one unit cell is modeled through traditional finite elements, as indicated in Fig. 7(b). The left boundary and right boundary of the unit cell are meshed with same number of DOFs. The dynamic equilibrium formulation of a unit cell can be written as:

$$\mathbf{K}\mathbf{u}(t) + \mathbf{C} \frac{\partial \mathbf{u}(t)}{\partial t} + \mathbf{M} \frac{\partial^2 \mathbf{u}(t)}{\partial t^2} = \mathbf{F}, \quad (38)$$

where \mathbf{K} and \mathbf{M} denote the stiffness matrix and mass matrix, respectively, $\mathbf{C} = \xi \mathbf{K} / \omega$ is identified as damping matrix considering damping lose factor ξ , \mathbf{u} is vectors of nodal displacement/rotation/torsion, \mathbf{F} represents force/moment/torque. Assuming that \mathbf{u} and \mathbf{F} are harmonic, the dynamic stiffness matrix will be written as $\mathbf{D} = \mathbf{K} + i\omega \mathbf{C} - \omega^2 \mathbf{M}$ in frequency (ω) domain. Eq. 38 can be re-expressed by dividing the DOFs into I (internal), L (left boundary) and R (right

boundary) DOFs, as described in Fig. 7(b), this yields:

$$\begin{bmatrix} \mathbf{D}_{LL} & \mathbf{D}_{LI} & \mathbf{D}_{LR} \\ \mathbf{D}_{IL} & \mathbf{D}_{II} & \mathbf{D}_{IR} \\ \mathbf{D}_{RL} & \mathbf{D}_{RI} & \mathbf{D}_{RR} \end{bmatrix} \begin{bmatrix} \mathbf{u}_{0L} \\ \mathbf{u}_{0I} \\ \mathbf{u}_{0R} \end{bmatrix} = \begin{bmatrix} \mathbf{F}_{0L} \\ \mathbf{F}_{0I} \\ \mathbf{F}_{0R} \end{bmatrix}. \quad (39)$$

where \mathbf{u}_0 and \mathbf{F}_0 are the amplitudes of \mathbf{u} and \mathbf{F} , respectively. It should be noticed that the internal DOFs are not affected by external loads due to the coupling actions are restricted to its left boundary and right boundary only [16], as a result, $\mathbf{F}_{0I} = 0$. The dynamic equilibrium equation, considering left boundary and right boundary in the matrix \mathbf{D} only, will be written as:

$$\begin{bmatrix} \mathbf{D}_{LL}^* & \mathbf{D}_{LR}^* \\ \mathbf{D}_{RL}^* & \mathbf{D}_{RR}^* \end{bmatrix} \begin{bmatrix} \mathbf{u}_{0L} \\ \mathbf{u}_{0R} \end{bmatrix} = \begin{bmatrix} \mathbf{F}_{0L} \\ \mathbf{F}_{0R} \end{bmatrix}, \quad (40)$$

where $\mathbf{D}^* = \mathbf{D}_{BB} - \mathbf{D}_{BI}\mathbf{D}_{II}^{-1}\mathbf{D}_{IB}$ is the condensed form of dynamic stiffness matrix, subscript B represents the DOFs on the boundaries of the unit cell. Note that this is a typical issue for WFEM [28] and a modal reduction can be applied to reduce the computational cost of the dynamic condensation. Eq. 40 is the starting point for the WFEM analysis that relates the displacement/rotation/torsion and force/moment/torque on the two sides of the unit cell. For the solution of propagation constants Λ and eigenvectors Ψ , one can solve the direct Bloch formulation [18, 29, 30] as:

$$\left[\mathbf{D}_{RL}^*(\omega)\Lambda^{-1} + \mathbf{D}_{RR}^*(\omega) + (\mathbf{D}_{LL}^*(\omega) + \mathbf{D}_{LR}^*(\omega)\Lambda) \right] \Psi = 0, \quad (41)$$

where $\Lambda = \text{diag}\{\lambda_j\}_{j=1,\dots,2m}$, $\Psi = \{\phi_j\}_{j=1,\dots,2m}$. The $2m$ eigenvalues in Eq. 41 can be divided into (λ_j, ϕ_j^+) and $(1/\lambda_j, \phi_j^-)$. The waves propagate to the positive direction if $|1/\lambda_j| < 1$. And the waves propagate to the negative direction if $|\lambda_j| > 1$. Here, λ_j take the form $\lambda_j = \exp(-i\kappa_j L_u)$. The direction of waves propagation can be defined utilizing $\Re(\kappa_j)$ when $|\lambda_j| = 1$ in the passing bands, which representing the real part of the wave-number. $\Re(\kappa_j) > 0$ means that the waves propagate to the positive direction. On the other hand, $\Re(\kappa_j) < 0$ represents that the waves propagate to the negative direction.

4. Numerical Applications

In this section, the WFEM is applied to study bending and torsional vibration based on SSG theory. Two different structures are considered for each: one is a single material structure with 5 unit cells, each unit cell's length L_u is $15a_0$ (a_0 is the lattice parameter) as shown in Fig. 8(a). The other one is a binary periodic structure with 5 unit cells, each unit cell has a length $L_u = 15a_0$ and consists of parts A and B as shown in Fig. 8(b). Both structures have a circular cross section with radius $r = 3a_0$ and loss factor $\xi = 1 \times 10^{-4}$.

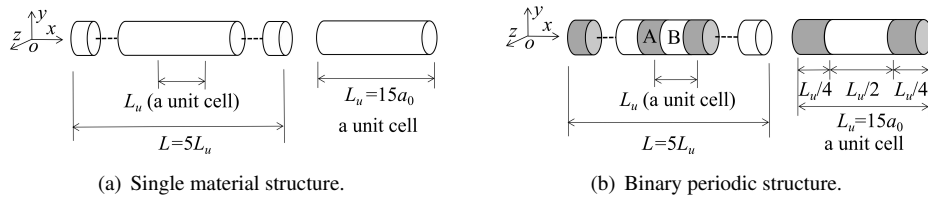


Figure 8: One-dimensional structures' configurations.

4.1. Bending Vibration

The bending vibration for single material and binary periodic structures are discussed. Aluminium (Al) is used for single material structure with linear mass density $\rho = 2.7 \text{ g/cm}^3$ and Young's modulus $E = 70 \text{ GPa}$, and each unit cell is divided into 100 elements. Al and Pb (Lead: linear mass density $\rho = 11.34 \text{ g/cm}^3$, Young's modulus $E = 16 \text{ GPa}$) are respectively used for part A with 50 elements and part B with 50 elements in binary periodic structure.

4.1.1. Single Material Structure

Firstly, the dispersion relation of a unit cell for single material Euler-Bernoulli beam is calculated by WFEM. The real part $\Re(\kappa_j)$ of wavenumber is the phase shift per unit length and the imaginary part $\Im(\kappa_j)$ means the attenuation per unit length. Only the positive waves with real and imaginary parts are illustrated due to the wavenumbers of the negative waves and positive waves are symmetric with respect to x -axis. The dimensionless wavenumbers in frequency range $[0, 30\omega_{b1}]$, where $\omega_{b1} = 3.516\sqrt{EI/\rho AL^4}$ [31] assumed as clamped-free boundary conditions, are presented in Fig. 9. There are four waves ($\kappa_1, \kappa_2, \kappa_3, \kappa_4$) predicted by SSG theory, in which κ_1 is non-classical bending wave propagating in a dispersive manner, κ_2 is the non-classical shear wave, κ_3 and κ_4 are the evanescent waves which exist exclusively in SSG theory.

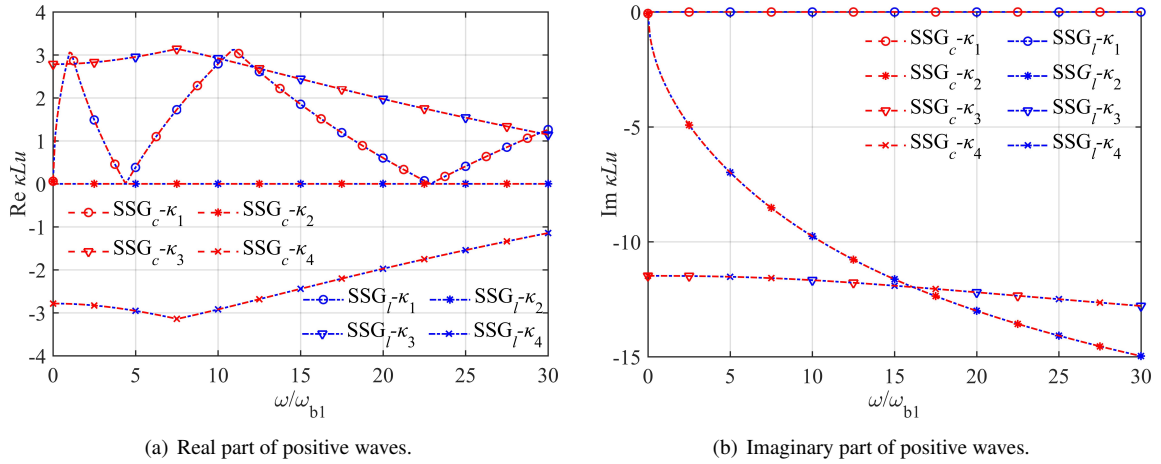


Figure 9: Dispersion relation for single material Euler-Bernoulli beam by SSG (ω_{b1} is the first nature frequency, subscript c of SSG means continuum model, l is lattice model).

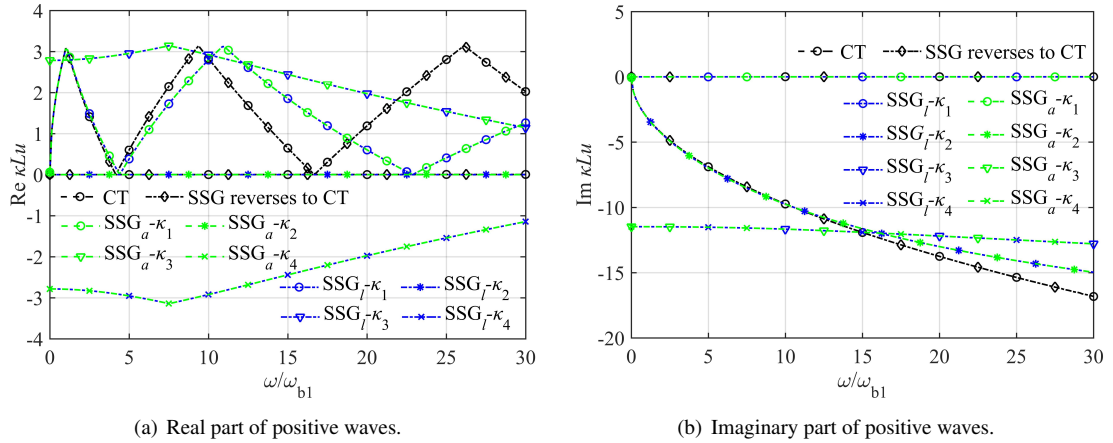


Figure 10: Comparison of dispersion relation between SSG and CT and reverse SSG to CT (subscript a of SSG means analytical method, l is lattice model).

In order to verify the WFEM results, an analytical method is used. Replacing displacement $w(x, t) = w_0 e^{i(\omega t - \kappa x)}$ into Eq. 9 assuming $f(x, t) = 0$, the analytical dynamical formulation of Euler-Bernoulli beam by SSG theory becomes: $B_1^b \kappa^4 + (B_4^b - B_2^b) \kappa^6 + B_3^b \kappa^8 = \rho A \omega^2$. The results by analytical method and WFEM via LSM are shown in Fig. 10. The dispersion relation by WFEM is in good accordance with the analytical method. On another hand, at low

frequency, κ_1 from SSG and CT are close, but a discrepancy appears at higher frequency. Note that without higher order material contributions (i.e. a_i, b_i and c_i equal 0), SSG becomes identical to CT.

Next, the forced response for single material Euler-Bernoulli beam is discussed, as presented in Fig. 8(a), the beam

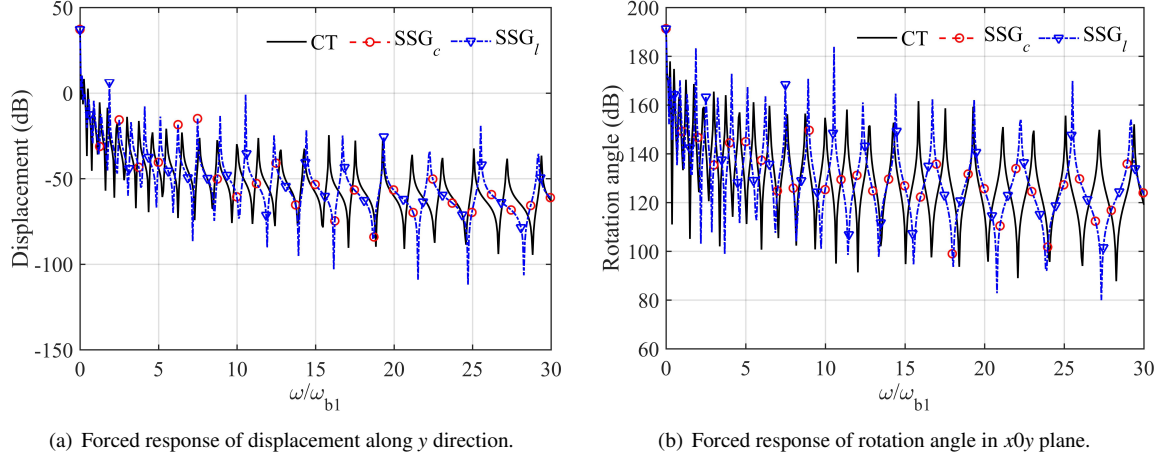


Figure 11: Forced response for single material Euler-Bernoulli beam by CT and SSG (subscript c means continuum model, l is lattice model).

consists of 5 unit cells. One side is clamped and another side is free and subjected to a harmonic force $f(x, t) = e^{i\omega t}$ on free end of the beam. The amplitude at free end is calculated out on each frequency according to Eq. 38. The forced response is shown in Fig. 11 by SSG theory and CT. It can be noticed that resonances are well predicted in both theories. Same as for the dispersion curves, the results show that discrepancies between CT and SSG FRF increase with frequency. Wave propagation is significantly affected by the micro-sized structure interactions. The input vibration energy can be transferred both by propagating waves and other evanescent waves, which decay rapidly in the near field of the excitation.

4.1.2. Periodic Structure

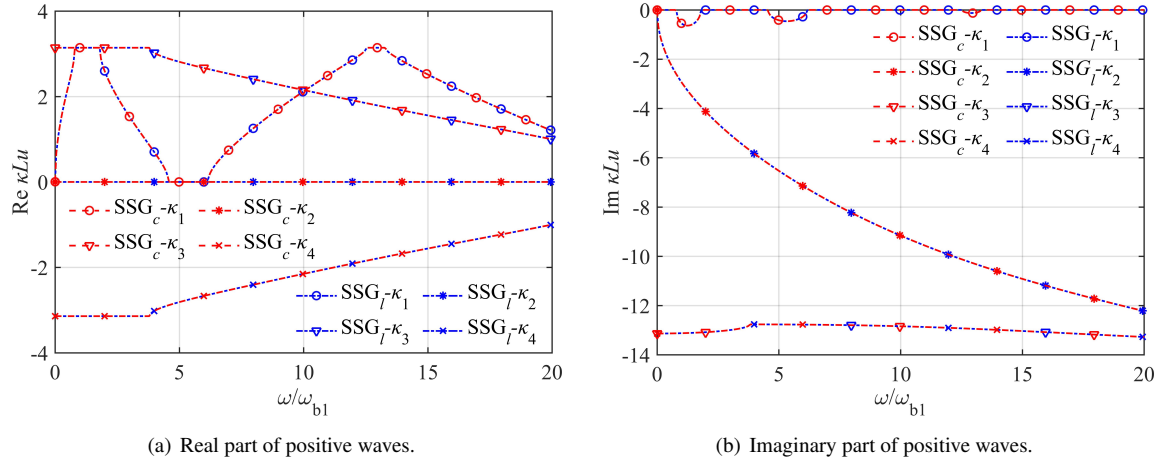


Figure 12: Dispersion relation for periodic Euler-Bernoulli beam by SSG (subscript c of SSG means continuum model, l is lattice model).

The dispersion relation with positive-going waves of a unit cell for periodic Euler-Bernoulli beam is calculated by WFEM. The dimensionless wavenumbers with real and imaginary parts of the waves $[0, 20\omega_{b1}]$ are presented in

Fig. 12. The difference with single material structures lies in the existence of stop bands (visible here on κ_1). For the bending wave in micro-sized periodic structure we have $\Re(\kappa_1) = 0$ within pass bands and $\Im(\kappa_1) \neq 0$ within stop bands, which is a typical behavior of evanescent waves. When $\Re(\kappa_1) = 0$, the waves decay exponentially with the stop bands frequencies bounded with $\lambda = 1$. The stop bands frequencies are bounded with $\lambda = -1$ which indicates a single wavelength when $\Re(\kappa_1) = \pm\pi/L_u$.

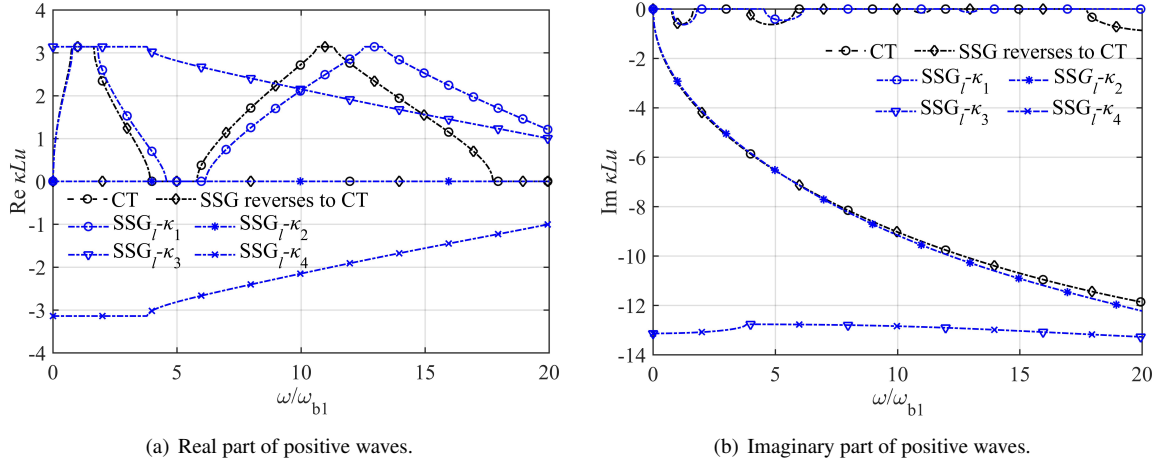


Figure 13: Comparison of dispersion relation between SSG and CT and reverse SSG to CT (subscript l of SSG means lattice model).

Next, the comparison between SSG theory and CT is shown in Fig. 13. It is noticed that at low frequency, the first wave by SSG confirms to CT well, but the difference is bigger when frequency increase. When higher order material parameters a_i, b_i and c_i are 0, SSG will reverse to CT.

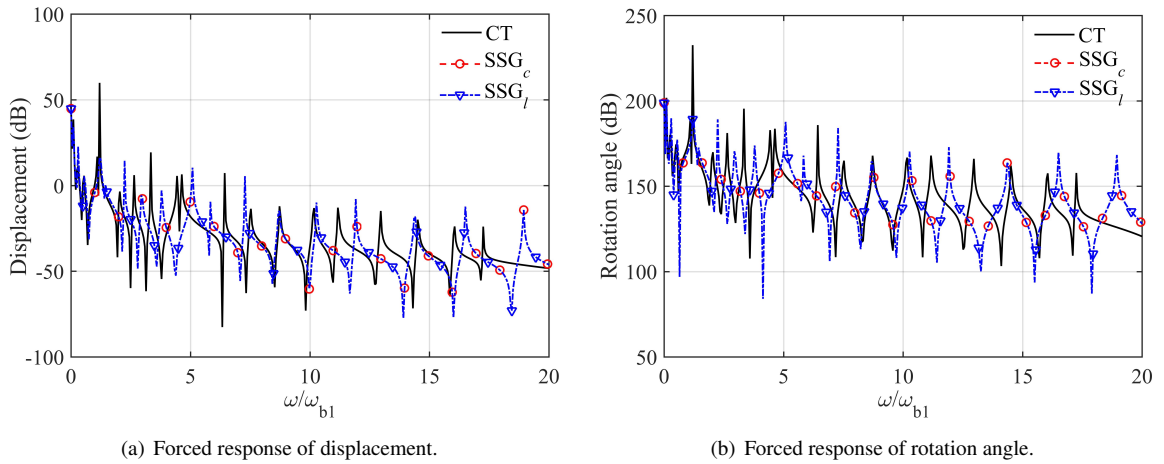


Figure 14: Forced response for periodic Euler-Bernoulli beam by CT and SSG (subscript c of SSG means continuum model, l denotes lattice model).

The forced response for periodic Euler-Bernoulli beam is discussed, as presented in Fig. 8(b), the beam is composed of 5 unit cells, each unit cell includes two parts with A and B. The boundary condition and external force are same as bending case of single material structure. The forced response of displacement and rotation angle is shown in Fig. 14 by SSG theory and CT. The resonances are predicted well by both theories. The results by these two theories close to each other at lower frequency range, but the values are different in higher frequency. The frequency ranges in the stop bands indicate that there is no resonance.

4.2. Torsional Vibration

Material Al with shear modulus $G = 26$ GPa is used for single material torsional bar with 100 elements in each unit cell. Al and Cu (shear modulus $G = 48$ GPa, linear mass density $\rho = 8.96$ g/cm³) are used for part A with 50 elements and part B with 50 elements in binary periodic bar, respectively.

4.2.1. Single Material Structure

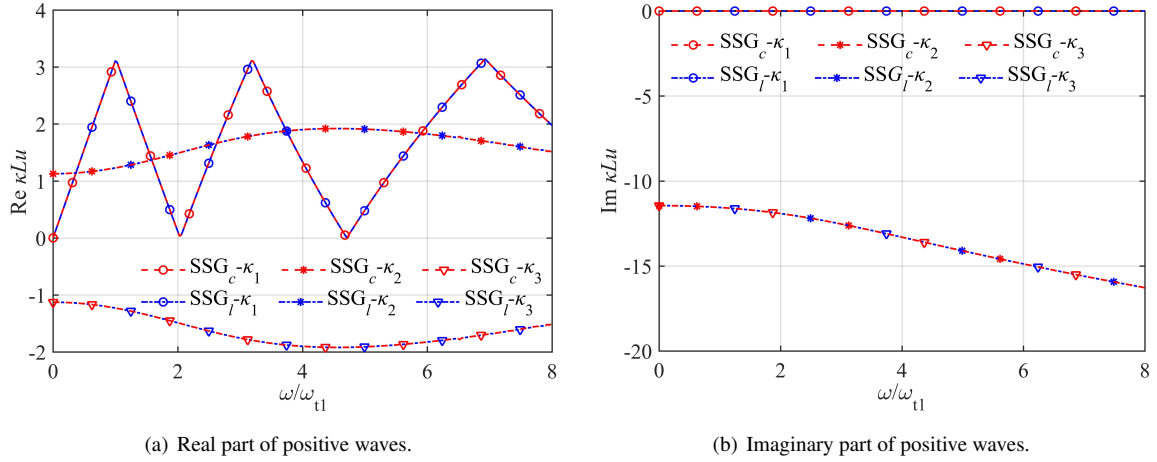


Figure 15: Dispersion relation for single material torsional bar by SSG ($\omega_{t1} = \pi \sqrt{G/4\rho L^2}$ [32] is the first nature frequency, subscript c of SSG means continuum model, l is lattice model).

Firstly, the dispersion relation of a unit cell for single material torsional bar is calculated by WFEM. The positive-going waves are shown in Fig. 15. Then, the WFEM is compared with the analytical method which expressed as $B_1^t \kappa^2 + (B_4^t - B_2^t) \kappa^4 + B_3^t \kappa^6 = \rho J \omega^2$. As shown in Fig. 16, the results indicate that there are three waves (κ_1 , κ_2 , κ_3) predicted by SSG theory, in which κ_1 is a dispersive non-classical torsional wave. The evanescent waves κ_2 and κ_3 exist only in SSG theory model. Next, the forced response is illustrated in Fig. 17 by SSG and CT. The boundary conditions are same as bending case of single material structure and a harmonic force $\bar{\Gamma}(x, t) = e^{i\omega t}$ is applied on free boundary of the bar. The characteristics of forced responses referred in the bending case of single material structure are observed in the torsional ones as well.

4.2.2. Periodic Structure

As presented in Fig. 18, the dispersion relation of a unit cell for periodic torsional bar is calculated by WFEM. And the comparison between SSG theory and CT is shown in Fig. 19. As we can see, the wave κ_1 of SSG confirms the wave of CT well when the frequency range is in the first pass band and stop band. But as the frequency increases, the difference between this two waves is getting bigger. This phenomena shows that the micro-sized structure's characteristics can be reflected by non-local theory at high frequency range. And when higher order material parameters a_i , b_i and c_i are 0, SSG will reverse to CT.

In this part, the forced response for periodic torsional bar is discussed by SSG theory and CT, as shown in Fig. 20. The boundary conditions and external force are same as single material structure of torsional bar. The frequency range can be divided into two parts, namely the stop bands frequency and pass bands frequency, and there is no resonances in stop bands. The results by these two theories match to each other just in the first pass and stop band frequency range.

5. Conclusions

In this paper, we used WFEM to study the dynamic behavior and wave propagation features of complex 1D micro-sized structures. The SSG theory is used to analyze the structural characteristics. The main contributions of the work

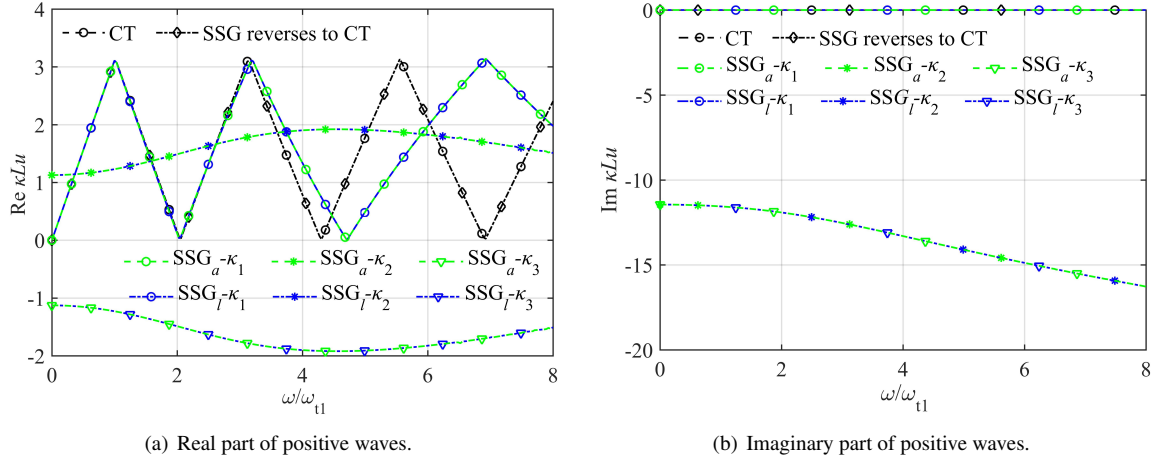


Figure 16: Comparison of dispersion relation between SSG and CT and reverse SSG to CT (subscript a means analytical method and l is lattice model).

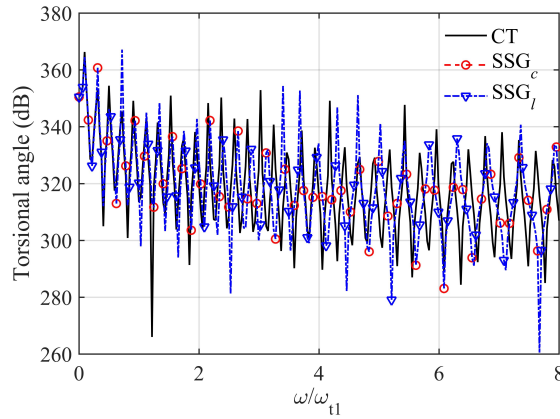


Figure 17: Forced response of single material torsional bar by CT and SSG (subscript c and l of SSG denote continuum model and lattice model, respectively).

are drawn as follows:

(i) The governing equations and boundary conditions of one-dimensional Euler-Bernoulli bending beam and torsional bar are derived from continuum models based on SSG theory. Then, two “non-local” Lattice Spring Models (LSM) for bending and torsion are introduced, and the dynamic equations from LSM are calculated respectively. Weak forms by SSG theory for bending and torsion are established finally. WFEM for one-dimensional structures is discussed. Free wave propagation characteristics are expressed by solving eigenvalue problems.

(ii) Bending and torsional dispersion relations for single material and binary periodic structures are presented by WFEM, respectively. For bending, there are four waves ($\kappa_1, \kappa_2, \kappa_3, \kappa_4$) predicted by SSG theory, in which κ_1 is non-classical bending wave propagating in a dispersive manner, κ_2 is non-classical shear wave, κ_3 and κ_4 are the evanescent waves which exist exclusively in SSG theory model. For torsion, there are three waves ($\kappa_1, \kappa_2, \kappa_3$) predicted by SSG theory, in which κ_1 is non-classical torsional wave propagating in a dispersive manner, κ_2 and κ_3 are the evanescent waves. Significant stop bands are observable for both bending and torsion modes in SSG periodic structures.

(iii) For the forced response of bending and torsion, wave propagation is significantly affected by the microstructure interactions. The input vibration energy can be transferred both by propagating waves and other evanescent waves which decay rapidly in the near field of the excitation.

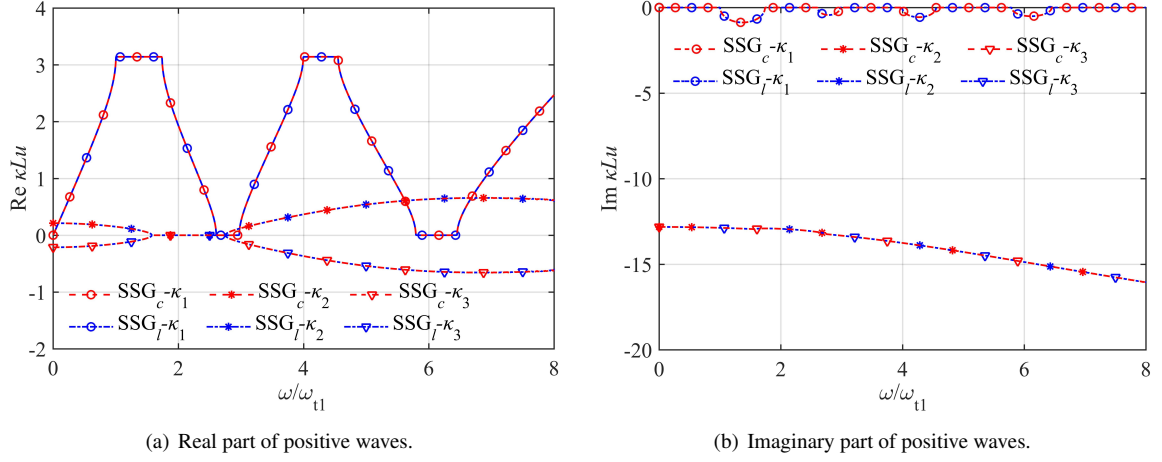


Figure 18: Dispersion relation for periodic torsional bar by SSG (subscript c of SSG means continuum model and l is lattice model).

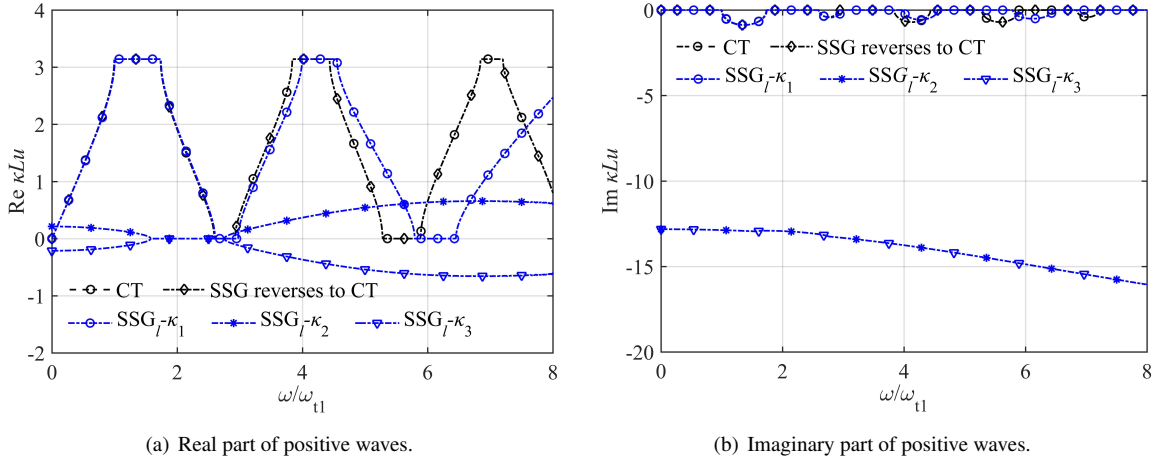


Figure 19: Comparison of dispersion relation between SSG and CT and reverse SSG to CT (subscript l of SSG means lattice model).

Acknowledgements

The research of B. Yang is funded by the LabEx CeLyA (Centre Lyonnais d'Acoustique, ANR-10-LABX-0060) of Université de Lyon. The research of C. Droz is funded by the European Commission (WIDEA) under the grant agreement No. 797034.

Appendix A. Transform Bending LSM to Continuum Model

The bending lattice equation of motion for particle n as:

$$\begin{aligned} & \frac{k_1}{d^3} (w_{n-2} - 4w_{n-1} + 6w_n - 4w_{n+1} + w_{n+2}) + \frac{k_2}{(2d)^3} (w_{n-4} - 4w_{n-2} + 6w_n - 4w_{n+2} + w_{n+4}) \\ & + \frac{k_3}{(3d)^3} (w_{n-6} - 4w_{n-3} + 6w_n - 4w_{n+3} + w_{n+6}) - F_n = M \frac{d^2 w_n(t)}{dt^2}. \end{aligned} \quad (\text{A.1})$$

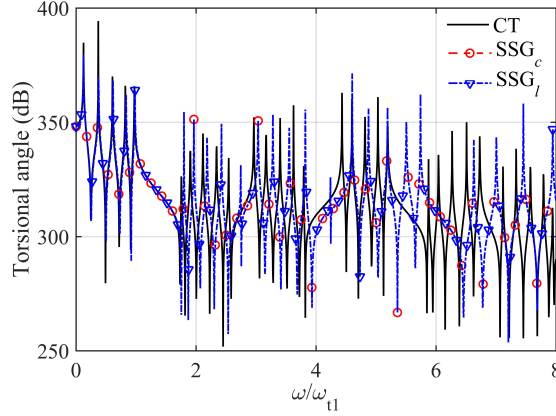


Figure 20: Forced response for periodic torsional bar by CT and SSG (subscript c of SSG means continuum model and l represents lattice model).

Multiplying Eq. (A.1) by e^{-iknd} , and summing over n from $-\infty$ to $+\infty$. Then Eq. (A.1) will be written as:

$$\begin{aligned}
& \frac{k_1}{d^3} \sum_{n=-\infty}^{+\infty} e^{-iknd} (w_{n-2} - 4w_{n-1} + 6w_n - 4w_{n+1} + w_{n+2}) + \frac{k_2}{(2d)^3} \sum_{n=-\infty}^{+\infty} e^{-iknd} (w_{n-4} - 4w_{n-2} \\
& + 6w_n - 4w_{n+2} + w_{n+4}) + \frac{k_3}{(3d)^3} \sum_{n=-\infty}^{+\infty} e^{-iknd} (w_{n-6} - 4w_{n-3} + 6w_n - 4w_{n+3} + w_{n+6}) \\
& - \sum_{n=-\infty}^{+\infty} e^{-iknd} F_n = M \sum_{n=-\infty}^{+\infty} e^{-iknd} \frac{d^2 w_n(t)}{dt^2}.
\end{aligned} \tag{A.2}$$

The first, second and third parts of the left side in Eq. (A.2) can be written as:

$$\begin{aligned}
& \frac{k_1}{d^3} \left(e^{-2ikd} \sum_{m=-\infty}^{+\infty} e^{-ikmd} w_m - 4e^{-ikd} \sum_{j=-\infty}^{+\infty} e^{-ikjd} w_j + 6 \sum_{n=-\infty}^{+\infty} e^{-iknd} w_n - 4e^{ikd} \sum_{p=-\infty}^{+\infty} e^{-ikpd} w_p \right. \\
& \left. + e^{2ikd} \sum_{q=-\infty}^{+\infty} e^{-ikqd} w_q \right) + \frac{k_2}{(2d)^3} \left(e^{-4ikd} \sum_{m=-\infty}^{+\infty} e^{-ikmd} w_m - 4e^{-2ikd} \sum_{j=-\infty}^{+\infty} e^{-ikjd} w_j + 6 \sum_{n=-\infty}^{+\infty} e^{-iknd} w_n \right. \\
& \left. - 4e^{2ikd} \sum_{p=-\infty}^{+\infty} e^{-ikpd} w_p + e^{4ikd} \sum_{q=-\infty}^{+\infty} e^{-ikqd} w_q \right) + \frac{k_3}{(3d)^3} \left(e^{-6ikd} \sum_{m=-\infty}^{+\infty} e^{-ikmd} w_m - 4e^{-3ikd} \sum_{j=-\infty}^{+\infty} e^{-ikjd} w_j \right. \\
& \left. + 6 \sum_{n=-\infty}^{+\infty} e^{-iknd} w_n - 4e^{3ikd} \sum_{p=-\infty}^{+\infty} e^{-ikpd} w_p + e^{6ikd} \sum_{q=-\infty}^{+\infty} e^{-ikqd} w_q \right).
\end{aligned} \tag{A.3}$$

Using the definition in Eq. (20), Eq. (A.3) will be written:

$$\begin{aligned}
& \frac{4k_1}{d^3} \left[-2 \sin^2 \left(\frac{\kappa d}{2} \right) \right]^2 \hat{w}(\kappa, t) + \frac{4k_2}{(2d)^3} \left[-8 \sin^2 \left(\frac{\kappa d}{2} \right) + 8 \sin^4 \left(\frac{\kappa d}{2} \right) \right]^2 \hat{w}(\kappa, t) \\
& + \frac{4k_3}{(3d)^3} \left[-18 \sin^2 \left(\frac{\kappa d}{2} \right) + 48 \sin^4 \left(\frac{\kappa d}{2} \right) - 32 \sin^6 \left(\frac{\kappa d}{2} \right) \right]^2 \hat{w}(\kappa, t).
\end{aligned} \tag{A.4}$$

Taylor series expansion is used here for sine function at the point 0 and limiting $d \rightarrow 0$ from Eq. (21). Then, substitution of Eq. (A.4) into Eq. (A.2) gives:

$$\begin{aligned} & G_4^b \kappa^4 \tilde{w}(\kappa, t) - G_6^b \kappa^6 \tilde{w}(\kappa, t) + G_8^b \kappa^8 \tilde{w}(\kappa, t) - \mathcal{O}(G_i^b \kappa^i \tilde{w}(\kappa, t)) - \mathfrak{F}(f(x, t)) \\ & = \rho A \frac{\partial^2 \tilde{w}(\kappa, t)}{\partial t^2}, (i = 10, 12, \dots), \end{aligned} \quad (\text{A.5})$$

with $G_4^b = k_1 + 2k_2 + 3k_3$, $G_6^b = -\left(\frac{k_1}{6} + \frac{4k_2}{3} + \frac{9k_3}{2}\right)d^2$, $G_8^b = \left(\frac{k_1}{80} + \frac{2k_2}{5} + \frac{243k_3}{80}\right)d^4$, $G_{10}^b = -\left(\frac{17k_1}{30240} + \frac{68k_2}{945} + \frac{1377k_3}{1120}\right)d^6, \dots$

The inverse Fourier transform \mathfrak{F}^{-1} of Eq. (A.5) has the form:

$$\begin{aligned} & G_4^b \mathfrak{F}^{-1}(\kappa^4 \tilde{w}(\kappa, t)) - G_6^b \mathfrak{F}^{-1}(\kappa^6 \tilde{w}(\kappa, t)) + G_8^b \mathfrak{F}^{-1}(\kappa^8 \tilde{w}(\kappa, t)) - \mathcal{O}\left(G_i^b \mathfrak{F}^{-1}(\kappa^i \tilde{w}(\kappa, t))\right) - f(x, t) \\ & = \rho A \frac{\partial^2 \mathfrak{F}^{-1}(\tilde{w}(\kappa, t))}{\partial t^2}. \end{aligned} \quad (\text{A.6})$$

The relations between the derivatives and its Fourier transforms, using the formula $\mathfrak{F}^{-1}(\tilde{w}(\kappa, t)) = w(x, t)$, can be written as:

$$\mathfrak{F}^{-1}(\kappa^4 \tilde{w}(\kappa, t)) = \frac{\partial^4 w(x, t)}{\partial x^4}, \quad \mathfrak{F}^{-1}(\kappa^6 \tilde{w}(\kappa, t)) = -\frac{\partial^6 w(x, t)}{\partial x^6}, \quad \mathfrak{F}^{-1}(\kappa^8 \tilde{w}(\kappa, t)) = \frac{\partial^8 w(x, t)}{\partial x^8}. \quad (\text{A.7})$$

As a result, the dynamic continuous equation $w(x, t)$ is obtained as:

$$G_4 \frac{\partial^4 w(x, t)}{\partial x^4} + G_6 \frac{\partial^6 w(x, t)}{\partial x^6} + G_8 \frac{\partial^8 w(x, t)}{\partial x^8} + \mathcal{O}\left(G_i \frac{\partial^i w(x, t)}{\partial x^i}\right) - f(x, t) = \rho A \frac{\partial^2 w(x, t)}{\partial t^2}. \quad (\text{A.8})$$

Appendix B. Governing Equation and Associated Boundary Conditions of a Torsional Bar by SSG Theory

Based on Eq. 27 and Eq. 28, \bar{u} (the strain energy density) of a torsional bar by SSG theory is expressed as:

$$\begin{aligned} \bar{u} = & \mu(\varepsilon_{21}^2 + \varepsilon_{12}^2 + \varepsilon_{13}^2 + \varepsilon_{31}^2) + a_3(\eta_{112}^2 + \eta_{113}^2) + a_4(\eta_{112}^2 + \eta_{113}^2 + \eta_{123}^2 + \eta_{213}^2 + \eta_{132}^2 + \eta_{312}^2) \\ & + a_5\eta_{213}\eta_{312} + b_4\zeta_{1132}\zeta_{1123} + b_5(\zeta_{1132}^2 + \zeta_{1123}^2 + \zeta_{1112}^2 + \zeta_{1113}^2) + b_6(\zeta_{3112}^2 + \zeta_{1312}^2 + \zeta_{1132}^2 \\ & + \zeta_{2113}^2 + \zeta_{1213}^2 + \zeta_{1123}^2 + \zeta_{1112}^2 + \zeta_{1113}^2) + b_7(\zeta_{3112}\zeta_{1123} + \zeta_{2113}\zeta_{1132}) + c_3(\varepsilon_{12}\zeta_{1112} + \varepsilon_{13}\zeta_{1113}), \end{aligned} \quad (\text{B.1})$$

Integrating strain energy density over its volume, the strain energy of the bar will be calculated as:

$$\mathcal{U} = \int_0^L \int_A \bar{u} dA dx'. \quad (\text{B.2})$$

By substitution of Eq. 28 and Eq. B.1 into Eq. B.2, the strain energy of the torsional bar by SSG theory is expressed as:

$$\mathcal{U} = \frac{1}{2} \int_0^L \left[B_1^t \left(\frac{\partial \varphi(x, t)}{\partial x} \right)^2 + B_2^t \left(\frac{\partial^2 \varphi(x, t)}{\partial x^2} \right)^2 + B_3^t \left(\frac{\partial^3 \varphi(x, t)}{\partial x^3} \right)^2 + B_4^t \frac{\partial \varphi(x, t)}{\partial x} \frac{\partial^3 \varphi(x, t)}{\partial x^3} \right] dx, \quad (\text{B.3})$$

where $B_1^t = GJ + 2A(4a_4 - a_5)$, $B_2^t = J(a_3 + a_4)/2 - 2A(b_4 + 2b_5 - 6b_6 + 2b_7)$, $B_3^t = 2J(b_5 + b_6)$, $B_4^t = Jc_3$, J means torsion of inertia within plane yOz .

The kinetic energy of the bar is presented as:

$$\mathcal{T} = \frac{1}{2} \int_0^L \rho J \left(\frac{\partial \varphi(x, t)}{\partial t} \right)^2 dx. \quad (\text{B.4})$$

The work done by external classical force and higher-order forces, W , can be established in the variation form as:

$$\delta^c W = \int_0^L \bar{\Gamma}(x, t) \delta \varphi dx + \Gamma_0 \delta \varphi(x, t)|_{x=0}^L + \Gamma_1 \delta \left(\frac{\partial \varphi(x, t)}{\partial x} \right) \Big|_{x=0}^L + \Gamma_2 \delta \left(\frac{\partial^2 \varphi(x, t)}{\partial x^2} \right) \Big|_{x=0}^L, \quad (\text{B.5})$$

where $\bar{\Gamma}(x, t)$ means the distributed torque within plane $y0z$, Γ_0 denotes the classical torque, $\Gamma_{1,2}$ are higher-order end-sectional torques of the micro-bar.

In this step, the Hamilton principle is used to calculate the strong forms of the bar for SSG theory as follows:

$$\int_{t_1}^{t_2} (\delta \mathcal{U} - \delta^c W - \delta \mathcal{T}) dt = 0, \quad (\text{B.6})$$

where $\delta \mathcal{U}$ and $\delta \mathcal{T}$ are the variation form of strain energy and kinetic energy, respectively. Then doing mathematical calculations according to the variation method by substituting equations Eq. B.3, Eq. B.4, and Eq. B.5 into Eq. B.6, one arrives at:

$$B_1^t \frac{\partial^2 \varphi(x, t)}{\partial x^2} + (B_4^t - B_2^t) \frac{\partial^4 \varphi(x, t)}{\partial x^4} + B_3^t \frac{\partial^6 \varphi(x, t)}{\partial x^6} - \bar{\Gamma}(x, t) = \rho J \frac{\partial^2 \varphi(x, t)}{\partial t^2}. \quad (\text{B.7})$$

Additionally, the associated boundary conditions for a torsional bar written as:

$$\begin{aligned} B_1^t \frac{\partial \varphi(x, t)}{\partial x} + (B_4^t - B_2^t) \frac{\partial^3 \varphi(x, t)}{\partial x^3} + B_3^t \frac{\partial^5 \varphi(x, t)}{\partial x^5} &= \Gamma_0 \quad \text{or} \quad \delta \varphi(x, t) = 0, \quad \text{on} \quad \Omega = \{0, L\}; \\ (B_2^t - \frac{1}{2} B_4^t) \frac{\partial^2 \varphi(x, t)}{\partial x^2} + B_3^t \frac{\partial^4 \varphi(x, t)}{\partial x^4} &= \Gamma_1 \quad \text{or} \quad \delta \frac{\partial \varphi(x, t)}{\partial x} = 0, \quad \text{on} \quad \partial \Omega; \\ \frac{1}{2} B_4^t \frac{\partial \varphi(x, t)}{\partial x} + B_3^t \frac{\partial^3 \varphi(x, t)}{\partial x^3} &= \Gamma_2 \quad \text{or} \quad \delta \frac{\partial^2 \varphi(x, t)}{\partial x^2} = 0 \quad \text{on} \quad \partial \Omega. \end{aligned} \quad (\text{B.8})$$

Appendix C. Transform Torsional LSM to Continuum Model

Multiplying Eq. (34) by e^{-iknd} with n from $-\infty$ to $+\infty$, Eq. (34) will be written as:

$$\begin{aligned} s_1 \sum_{n=-\infty}^{+\infty} e^{-iknd} (\varphi_{n-1} - 2\varphi_n + \varphi_{n+1}) + s_2 \sum_{n=-\infty}^{+\infty} e^{-iknd} (\varphi_{n-2} - 2\varphi_n + \varphi_{n+2}) \\ + s_3 \sum_{n=-\infty}^{+\infty} e^{-iknd} (\varphi_{n-3} - 2\varphi_n + \varphi_{n+3}) - \sum_{n=-\infty}^{+\infty} e^{-iknd} \Gamma_n &= \frac{mJ}{A} \sum_{n=-\infty}^{+\infty} e^{-iknd} \frac{d^2 \varphi_n(t)}{dt^2}. \end{aligned} \quad (\text{C.1})$$

The first, second and third parts on the right side in Eq. (C.1) are:

$$\begin{aligned} s_1 (e^{-ikd} \sum_{j=-\infty}^{+\infty} e^{-ikjd} \varphi_j - 2 \sum_{n=-\infty}^{+\infty} e^{-iknd} \varphi_n + e^{-ikd} \sum_{p=-\infty}^{+\infty} e^{-ikpd} \varphi_p) \\ + s_2 (e^{-2ikd} \sum_{j=-\infty}^{+\infty} e^{-ikjd} \varphi_j - 2 \sum_{n=-\infty}^{+\infty} e^{-iknd} \varphi_n + e^{-2ikd} \sum_{p=-\infty}^{+\infty} e^{-ikpd} \varphi_p) \\ + s_3 (e^{-3ikd} \sum_{j=-\infty}^{+\infty} e^{-ikjd} \varphi_j - 2 \sum_{n=-\infty}^{+\infty} e^{-iknd} \varphi_n + e^{-3ikd} \sum_{p=-\infty}^{+\infty} e^{-ikpd} \varphi_p). \end{aligned} \quad (\text{C.2})$$

Using the definition of Eq. (20) (replace $w(x, t)$ with $\varphi(x, t)$), Eq. (C.2) gives:

$$\begin{aligned} & s_1 \left(e^{-ikd} \widehat{\varphi}(\kappa, t) - 2\widehat{\varphi}(\kappa, t) + e^{-ikd} \widehat{\varphi}(\kappa, t) \right) + s_2 \left(e^{-2ikd} \widehat{\varphi}(\kappa, t) - 2\widehat{\varphi}(\kappa, t) + e^{-2ikd} \widehat{\varphi}(\kappa, t) \right) \\ & + s_3 \left(e^{-3ikd} \widehat{\varphi}(\kappa, t) - 2\widehat{\varphi}(\kappa, t) + e^{-3ikd} \widehat{\varphi}(\kappa, t) \right) \\ & = - (2s_1 + 16s_2 + 36s_3) \sin^2 \frac{\kappa d}{2} \widehat{\varphi}(\kappa, t) + (16s_2 + 96s_3) \sin^4 \frac{\kappa d}{2} \widehat{\varphi}(\kappa, t) - 64s_3 \sin^6 \frac{\kappa d}{2} \widehat{\varphi}(\kappa, t). \end{aligned} \quad (C.3)$$

Taylor series expansion is used here for sine function at the point 0 and transit to the limit $d \rightarrow 0$ from Eq. (21), substitution of Eq. (C.3) into Eq. (C.1) gives::

$$\begin{aligned} & -G_2^t k^2 \tilde{\varphi}(\kappa, t) + G_4^t k^4 \tilde{\varphi}(\kappa, t) - G_6^t k^6 \tilde{\varphi}(\kappa, t) + O\left(G_i^t k^i \tilde{\varphi}(\kappa, t)\right) - \mathfrak{F}(\bar{\Gamma}(x, t)) \\ & = \rho J \frac{\partial^2 \tilde{\varphi}(\kappa, t)}{\partial t^2}, (i = 8, 10, \dots), \end{aligned} \quad (C.4)$$

with $G_2^t = (s_1 + 4s_2 + 9s_3)d$, $G_4^t = \left(\frac{s_1}{12} + \frac{4s_2}{3} + \frac{27s_3}{4}\right)d^3$, $G_6^t = \left(\frac{s_1}{360} + \frac{8s_2}{54} + \frac{81s_3}{40}\right)d^5$, $G_8^t = \left(\frac{7s_1}{20160} + \frac{4s_2}{315} + \frac{729s_3}{2240}\right)d^7, \dots$

The form of inverse Fourier transform \mathfrak{F}^{-1} from Eq. (22) (replace w with φ) is expressed as:

$$\begin{aligned} & -G_2^t \mathfrak{F}^{-1}(k^2 \tilde{\varphi}(\kappa, t)) + G_4^t \mathfrak{F}^{-1}(k^4 \tilde{\varphi}(\kappa, t)) - G_6^t \mathfrak{F}^{-1}(k^6 \tilde{\varphi}(\kappa, t)) + O\left(G_i^t \mathfrak{F}^{-1}(k^i \tilde{\varphi}(\kappa, t))\right) - \bar{\Gamma}(x, t) \\ & = \rho J \frac{\partial^2 \mathfrak{F}^{-1}(\tilde{\varphi}(\kappa, t))}{\partial t^2}, (i = 8, 10, \dots). \end{aligned} \quad (C.5)$$

The relations between the derivatives and its Fourier transforms, using $\mathfrak{F}^{-1}(\tilde{\varphi}(\kappa, t)) = \varphi(x, t)$, can be expressed as:

$$\mathfrak{F}^{-1}(k^2 \tilde{\varphi}(\kappa, t)) = -\frac{\partial^2 \varphi(x, t)}{\partial x^2}, \quad \mathfrak{F}^{-1}(k^4 \tilde{\varphi}(\kappa, t)) = \frac{\partial^4 \varphi(x, t)}{\partial x^4}, \quad \mathfrak{F}^{-1}(k^6 \tilde{\varphi}(\kappa, t)) = -\frac{\partial^6 \varphi(x, t)}{\partial x^6}. \quad (C.6)$$

As a result, the dynamic continuous equation $\varphi(x, t)$ is obtained as:

$$\begin{aligned} & G_2^t \frac{\partial^2 \varphi(x, t)}{\partial x^2} + G_4^t \frac{\partial^4 \varphi(x, t)}{\partial x^4} + G_6^t \frac{\partial^6 \varphi(x, t)}{\partial x^6} + O\left(G_i^t \frac{\partial^i \varphi(x, t)}{\partial x^i}\right) - \bar{\Gamma}(x, t) \\ & = \rho J \frac{d^2 \varphi(x, t)}{dt^2}, (i = 8, 10, \dots). \end{aligned} \quad (C.7)$$

References

- [1] H. Askes, E. C. Aifantis, Gradient elasticity in statics and dynamics: an overview of formulations, length scale identification procedures, finite element implementations and new results, *International Journal of Solids and Structures* 48 (2012) 1962–1990.
- [2] S. Momeni, M. Asghari, The second strain gradient functionally graded beam formulation, *Composite Structures* 188 (2018) 15–24.
- [3] G. Zhu, C. Droz, A. M. Zine, M. N. Ichchou, Wave propagation analysis for a second strain gradient rod theory, *Chinese Journal of Aeronautics* (2019). doi:10.1016/j.cja.2019.10.006.
- [4] B. I. Halperin, Quantized hall conductance, current-carrying edge states, and the existence of extended states in a two-dimensional disordered potential, *Physical review B* 25 (4) (1982) 2185.
- [5] B. A. Bernevig, T. L. Hughes, S. C. Zhang, Quantum spin hall effect and topological phase transition in hgte quantum wells, *Science* 314 (5806) (2006) 57–61.
- [6] R. E. Miller, V. B. Shenoy, Size-dependent elastic properties of nano-sized structural elements, *Nanotechnology* 11 (3) (2000) 139.
- [7] C. W. Lim, L. H. He, Size-dependent nonlinear response of thin elastic films with nano-scale thickness, *International Journal of Solids and Structures* 46 (11) (2004) 15–26.
- [8] M. E. Gurtin, A. I. Murdoch, A continuum theory of elastic material surfaces, *Archive for rational mechanics and analysis* 57 (4) (1975) 291–323.
- [9] A. C. Eringen, Vistas of nonlocal continuum physics, *International Journal of Engineering* 30 (1992) 1551–1565.
- [10] M. E. Gurtin, A. I. Murdoch, A continuum theory of elastic material surfaces, *Archive for Rational Mechanics and Analysis* 57 (4) (1975) 291–323.
- [11] R. D. Mindlin, Second gradient of strain and surface tension in linear elasticity, *International Journal of Solids and Structures* (1965) 147–438.
- [12] R. D. Mindlin, N. N. Eshel, On first strain gradient theories in linear elasticity, *International Journal of Solids and Structures* (1968) 109–124.

- [13] R. A. Toupin, D. C. Gazis, Proceedings of the international conference on lattice dynamics, Copenhagen (1963).
- [14] A. Lazarus, O. Thomas, J.-F. Deu, Finite element reduced order models for nonlinear vibrations of piezoelectric layered beams with applications to nems, *Finite Elements in Analysis and Design* 49 (2012) 35–51.
- [15] Q. T. Aten, B. D. Jensen, L. L. Howell, Geometrically non-linear analysis of thin-film compliant mems via shell and solid elements, *Finite Elements in Analysis and Design* 49 (2012) 70–77.
- [16] D. Mead, A general theory of harmonic wave propagation in linear periodic systems with multiple coupling, *Journal of Sound and Vibration* 27 (1973) 235–260.
- [17] J. M. Mencik, M. N. Ichchou, Wave finite elements in guided elastodynamics with internal fluid, *International Journal of Solids and Structures* 44 (2007) 2148–2167.
- [18] C. Droz, J. P. Lainé, M. N. Ichchou, G. Inquiété, A reduced formulation for the free-wave propagation analysis in composite structures, *Composite Structures* 113 (2014) 134–144.
- [19] D. Duhamel, B. R. Mace, M. Brennan, Finite element analysis of the vibrations of waveguides and periodic structures, *Journal of Sound and Vibration* 294 (2006) 205–220.
- [20] V. Thierry, L. Brown, D. Chronopoulos, Multi-scale wave propagation modelling for two-dimensional periodic textile composites, *Composites Part B: Engineering* 150 (2018) 144–156.
- [21] Q. Serra, M. Ichchou, J.-F. Deü, Wave properties in poroelastic media using a wave finite element method, *Journal of Sound and Vibration* 335 (2015) 125–146.
- [22] W. Zhou, M. Ichchou, Wave propagation in mechanical waveguide with curved members using wave finite element solution, *Computer Methods in Applied Mechanics and Engineering* 199 (2010) 2099–2109.
- [23] H. M. Shodja, F. Ahmadpoor, T. A., Calculation of the additional constants for fcc materials in second strain gradient elasticity: behavior of a nano-size bernoulli-euler beam with surface effects, *Applied Mechanics* 72 (2) (2010) 021008.
- [24] M. Attar, A. Karrech, K. Regenauer Lieb, Non-linear analysis of beam-like structures on unilateral foundations: A lattice spring model, *International Journal of Solids and Structures* 88 (2016) 192–214.
- [25] V. E. Tarasov, Continuous limit of discrete systems with long-range interaction, *Journal of Physics A* 39 (48) (2006) 14895–14910.
- [26] V. E. Tarasov, Lattice with long-range interaction of power-law type for fractional non-local elasticity, *International Journal of Solids and Structures* 51 (2014) 2900–2907.
- [27] H. Askes, E. C. Aifantis, Gradient elasticity in statics and dynamics: An overview of formulations, length scale identification procedures, finite element implementations and new results, *International Journal of Solids and Structures* 48 (2011) 1962–1990.
- [28] C. Droz, C. Zhou, M. Ichchou, J.-P. Lainé, A hybrid wave-mode formulation for the vibro-acoustic analysis of 2d periodic structures, *Journal of Sound and Vibration* 363 (2016) 285–302.
- [29] V. Serey, N. Quaegebeur, P. Micheau, P. Masson, M. Castaings, M. Renier, Selective generation of ultrasonic guided waves in a bi-dimensional waveguide, *Structural Health Monitoring* 18 (2019) 1324–1336.
- [30] B. R. Mace, D. Duhamel, M. J. Brennan, L. Hinke, Finite element prediction of wave motion in structural waveguides, *Journal of the Acoustical Society of America* 117 (2005) 2835–2843.
- [31] M. Avcar, Free vibration analysis of beams considering different geometric characteristics and boundary conditions, *International Journal of Mechanics and Applications* 4 (3) (2014) 94–100.
- [32] S. S. Rao, *Vibration of continuous systems*, Wiley, New Jersey, 2007, Ch. Torsional vibration of shafts, pp. 280–282.